Title
HEAVY-ION ELASTIC SCATTERING

Author
Alster, Jonas.

Publication Date
1961-04-17

UCRL-9650
cy2

University of California

Ernest O. Lawrence Radiation Laboratory

Berkeley, California

UCRL-9650
UC-34 Physics
TID-4500 (16th Ed.)

UNIVERSITY OF CALIFORNIA
Lawrence Radiation Laboratory
Berkeley, California
Contract No. W-7405-eng-48

HEAVY-ION ELASTIC SCATTERING

Jonas Alster
(Ph.D. Thesis)

April 17, 1961

Printed in USA. Price $2.00. Available from the
Office of Technical Services
U. S. Department of Commerce
Washington 25, D.C.

HEAVY-ION ELASTIC SCATTERING

Contents

Appendices

HEAVY-ION ELASTIC SCATTERING

Jonas Alster

Lawrence Radiation Laboratory
University of California
Berkeley, California

April 17, 1961

ABSTRACT

The elastic scattering of C^{12} ions from A, Fe, Ni, Ag^{107}, In and Ta has been measured as a function of angle, at a laboratory-system energy of 124.5 Mev with the Berkeley heavy-ion linear accelerator. The experimental equipment and techniques are discussed. The angular distributions show the same general behavior as previous heavy-ion elastic scattering experiments. The experimental data were analyzed with the semiclassical Blair model as modified by McIntyre. Very good agreement with experiment was obtained. The measurements were taken with 1% statistics in order to study the structure of the angular distributions in greater detail, because only by fitting the details in the structure was it possible to obtain unambiguous sets of parameters. These parameters indicated a nuclear radius of $1.45A^{1/3} \times 10^{-13}$ cm, and a nearly constant surface thickness of 1.6×10^{-13} cm. Also, total reaction cross sections were obtained. A rainbow-model analysis by Goldman of the present data is given. Existing α- and heavy-ion scattering data have been analyzed with the McIntyre model and compared with previous optical-model analyses of the same data. It was found that, by independent analysis, the two models give the same imaginary phase shifts for all partial waves. The real phase shifts are identical above a certain ℓth partial wave, but differ widely below this ℓ value. It is shown that in the region of disagreement the real part of the phase shifts is irrelevant to the calculation of the cross section.

I. INTRODUCTION

One of the most interesting aspects of the use of heavy ions in nuclear research is that semiclassical arguments can be used to explain some of their interactions with nuclei. The criterion for the validity of classical argument is that the wave packet describing the particle should be small in comparison with the dimensions of interest; for coulomb scattering, one thus requires that the wave length connected with the relative motion be small compared with the distance of closest approach for a head-on collision, i.e.,

$$\lambdabar [Z_1 Z_2 e^2/E]^{-1} \ll 1 \text{ or } n = Z_1 Z_2 e^2/\hbar v \gg 1 ,$$

where Z_1 is the charge of the projectile,
Z_2 is the charge of the target,
e is the electronic charge,
$\hbar$ is Planck's constant divided by 2π, and
v is the relative velocity.

The parameter n is important in all calculations involving Coulomb interactions. For past elastic α-scattering experiments, n has usually been in the range 1 to 10, and semiclassical arguments have been very successful in explaining them, especially Blair's sharp-cutoff model.[2, 3, 4, 5] For heavy ions, n can be in the range 10 to 30. This larger value of the classical parameter suggests that the Blair model should hold even better for heavy ions.

Many important fields of nuclear research were enlarged when heavy-ion beams became available, such as that of Coulomb excitation, where strong electromagnetic interactions can be produced by heavy ions with energies below the Coulomb barrier, and in the production of neutron-deficient isotopes for studies in nuclear spectroscopy. When a heavy ion hits a nucleus it can impart to the nucleus from 50 to 100 units of angular momentum. If a compound nucleus is formed with such a high angular momentum, interesting problems arise in the nature of its decay. Several reviews on heavy-ion research can be found in the literature,[6-10] but here only elastic scattering experiments are discussed. As Blair pointed out,[5,8] through these experiments one hopes to gather general information on heavy-ion interactions, and in particular to learn something about the nuclear surface. Blair therefore suggested that a systematic survey be made throughout the periodic table to measure the nuclear radius, especially since some α-scattering data indicated some irregularities in the radius of nuclei around Pb^{208}.[3]

A. The Blair Model

Rutherford's formula for Coulomb scattering of two point charges gives the differential cross section as follows:[11]

$$\frac{d\sigma(\theta)}{d\Omega} = \left(\frac{Z_1Z_2e^2}{4E}\right)^2 \frac{1}{\sin^4\frac{1}{2}\theta} \qquad (1.1)$$

where $d\sigma(\theta)/d\Omega$ is the probability for scattering at angle θ into a unit solid angle, and E is the c.m. (center-of-mass) energy.

How does this formula change when the charges occur on spheres of finite dimensions? We discuss this problem using Fig. 1.

The impact parameter b is given by[11]

$$b = (Z_1Z_2e^2/mv^2)\cot\frac{1}{2}\theta\,, \qquad (1.2)$$

and the classical angular momentum by

$$\ell_c = (Z_1Z_2e^2/v)\cot\frac{1}{2}\theta\,. \qquad (1.3)$$

The distance of closest approach D is

$$D = (Z_1Z_2e^2/2E)\,(1+\operatorname{cosec}\frac{1}{2}\theta) \qquad (1.4)$$

Evidently, this distance may not be less than the sum R of the radii of the two charges; equating D with R in Eq.(1.4), and combining with (1.3), we thus find a critical angular momentum ℓ':

$$\ell'^2 = 2mR^2\,(E - Z_1Z_2e^2/R). \qquad (1.5)$$

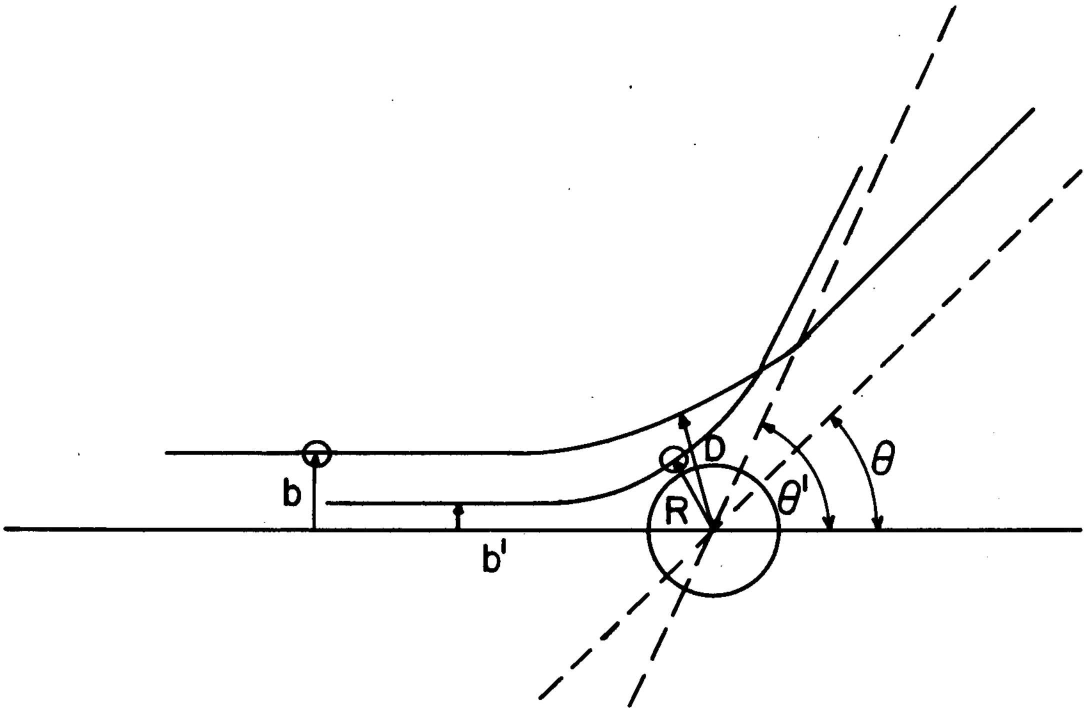

MU-23579

Fig. 1. Classical Coulomb trajectories and scattering parameters.

The Blair model now assumes that all particles with higher angular momentum pass the nucleus along the Coulomb trajectories, but that all particles with lower angular momentum are absorbed from the incident beam. Thus, classically speaking, the scattering will be described by the Rutherford formula for angles smaller than the critical angle corresponding to ℓ', and no scattering at larger angles will occur.

In order to see in a somewhat more refined way how this assumption affects that scattering formula (1.1), we develop the scattered beam in partial waves, [12]

$$f(\theta) = \frac{\lambda}{2i} \sum_{\ell=0}^{\infty} (2\ell+1)(\eta_\ell - 1) P_\ell(\cos\theta), \qquad (1.6)$$

in which η_ℓ is the coefficient of the ℓth scattered wave, and for Coulomb scattering of point charges,

$$\eta_\ell = \exp[2i\sigma_\ell] \; ; \; \sigma_\ell = \arg\Gamma(1+\ell+in) \qquad (1.7)$$

(n having been previously defined). The Rutherford formula can be obtained by inserting (1.7) into (1.6) and remembering that $d\sigma(\theta)/d\Omega = |f(\theta)|^2$. The imaginary part of the amplitude of the scattered ℓ waves for this case has been plotted in Fig. 2 for different scattering angles θ and a value $n = 22$.

The scattering formula in the Blair model is now obtained by subtracting from the Coulomb scattering all contributions of partial waves with angular momenta smaller than the critical one given by Eq. (1.5), or better, its quantum mechanical analogue:

$$\hbar^2 \ell'(\ell'+1) = 2mR^2 (E - Z_1 Z_2 e^2/R) . \qquad (1.8)$$

The ratio of the differential cross section obtained in this way to the Rutherford cross section is

$$\frac{\sigma(\theta)}{\sigma_R(\theta)} = \Big\{ \sin(n \ln \sin^2 \tfrac{1}{2}\theta) +$$

$$+\frac{\sin^2\frac{1}{2}\theta}{n}\sum_{\ell=0}^{\ell'}(2\ell+1)\sin 2(\sigma_\ell-\sigma_0)P_\ell(\cos\theta)\Biggr\}^2 +$$

$$+\Biggl\{\cos(n\ln\sin^2\tfrac{1}{2}\theta)+$$

$$+\frac{\sin^2\frac{1}{2}\theta}{n}\sum_{\ell=0}^{\ell'}(2\ell+1)\cos 2(\sigma_\ell-\sigma_0)P_\ell(\cos\theta)\Biggr\}^2, \qquad (1.9)$$

as is shown in Appendix A.

Two angular distributions calculated with this formula are given in Fig. 3, together with the experimentally measured angular distributions.

The main features of the angular distributions can be qualitatively explained very well with Fig. 1 and 2. Figure 2 shows that there is a large group of amplitudes with the same sign, centered around ℓ_c. This group provides the main contribution to the Rutherford scattering for this particular angle. For small angles, ℓ_c becomes larger and the main group of amplitudes moves along with it. The amplitudes below ℓ' are cut off and, since ℓ' is fixed, different amplitudes are cut off for different angles. If ℓ' coincides with ℓ_c, about half of the main ℓ waves are cut off; so at that angle the cross section should be about 1/4 of the Coulomb cross section given by Equation (1.1).

The Blair quarter-point recipe for the measurement of radii is based on this picture.^{3} For small angles, the main group of amplitudes is completely included in the sum, and the cross section does not differ very much from the Coulomb cross section. A drop in cross section occurs after ℓ waves of the large coherent group are cut off. A consistent feature of the angular distributions is the rise above Rutherford scattering before the steep dropoff. The Blair model reproduces this rise, the nature of which can again be explained with Fig. 2. Before the main group of amplitudes there is always a smaller group of amplitudes of opposite sign. When by increasing ℓ_c this group is cut off at ℓ', negative amplitudes are subtracted, resulting in a larger positive sum, which will therefore give a larger cross section.

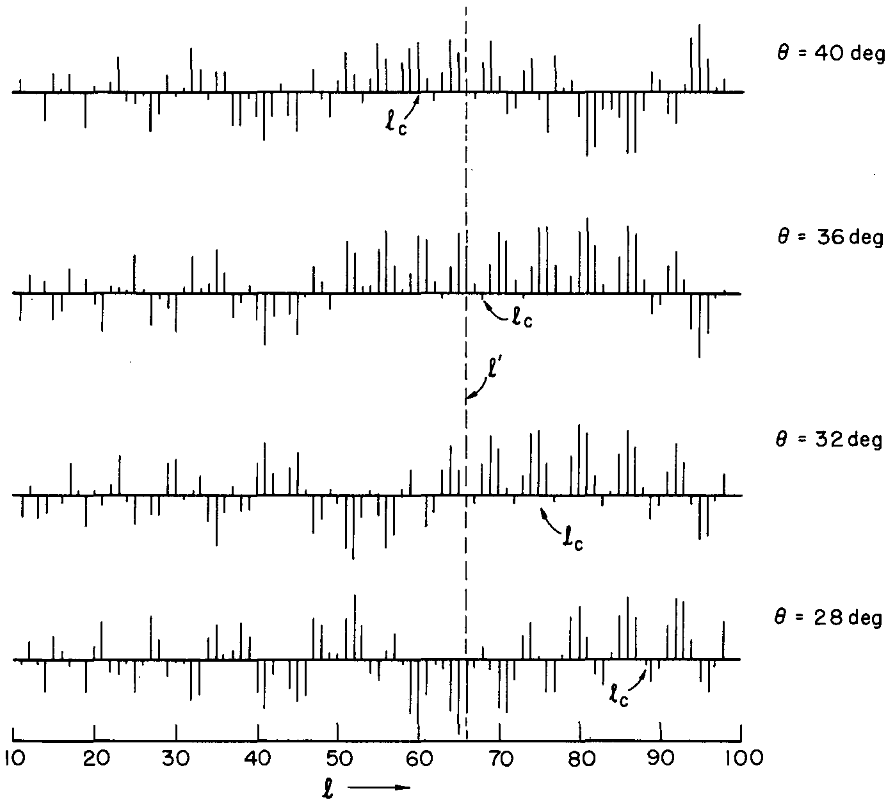

MU-23525

Fig. 2. The imaginary part of the amplitude of outgoing ℓ waves for a Coulomb potential: $(2\ell + 1) \cos 2 (\sigma_\ell - \sigma_0) P_\ell (\cos \theta)$ for n = 22, for different angles.

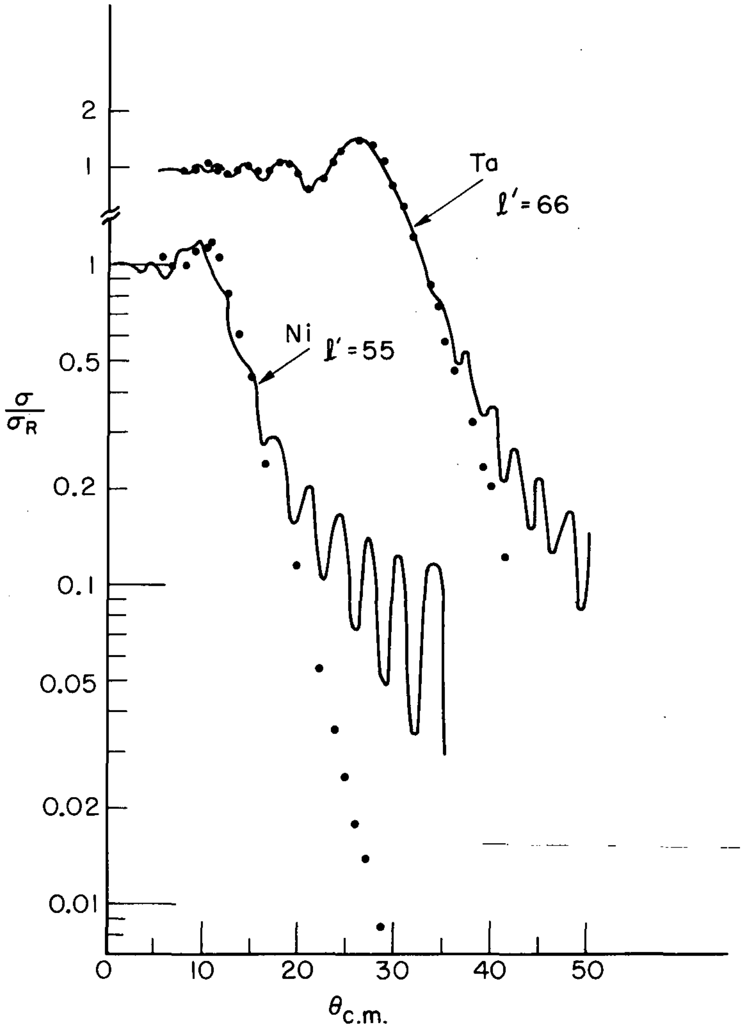

MU-23521

Fig. 3. The differential cross section divided by the Rutherford cross section as a function of the center-of-mass angle (in degrees) is plotted for C^{12} elastically scattered from Ta and Ni. The dots are the experimental values and the solid line is the Blair sharp-cutoff calculation.

We now compare experimental cross sections with the cross sections calculated with Formula (1.9). By changing only one parameter, ℓ', a best fit is obtained. The best value for ℓ' is substituted into Eq. (1.8) which in turn gives a value for R equal to $R_{\text{nucleus}} + R_{\text{projectile}}$. Usually an unambiguous choice in ℓ' can be made of the order of 60 to 70, such that the precision with which R is found depends only on the precision of E in Eq. (1.8). Since the energy spread in these experiments is somewhat less than 1%, the interaction radius R can be found with a precision of 1%. Such precision for measuring nuclear radii can be matched only with electron scattering experiments; the last ones measure, however, a "nuclear charge radius" rather than the "nuclear mass radius" measured in the above mentioned work.

B. A Modified Blair Model

The Blair model describes the data quite well, which is somewhat surprising in view of its simple classical nature, but also it gives rise to large oscillations for small $(d\sigma(\theta)/d\Omega)/(d\sigma(\theta)/d\Omega)_R$, whereas the experimental cross sections decrease smoothly in an exponential way. The strong oscillations arise because of the extreme sharp cutoff at one particular radius. Blair predicted that a rounding of the cutoff would smooth out the oscillations. Several attempts have been made to modify the Blair model.[13-15] The first successful modification was introduced by McIntyre to explain some elastic α-scattering data.[15] The rounding is obtained by changing the coefficient of the scattered partial waves $\eta_\ell = A_\ell \exp[2i(\sigma_\ell + \delta_\ell)]$ through the arbitrary relations

$$A_\ell = \left\{1 + \exp\left[(\ell_A - \ell)/\Delta\ell_A\right]\right\}^{-1}$$

$$\delta_\ell = \delta_0 \left\{1 + \exp\left[(\ell - \ell_\delta)/\Delta\ell_\delta\right]\right\}^{-1} \qquad (1.10)$$

(see Fig. 4).

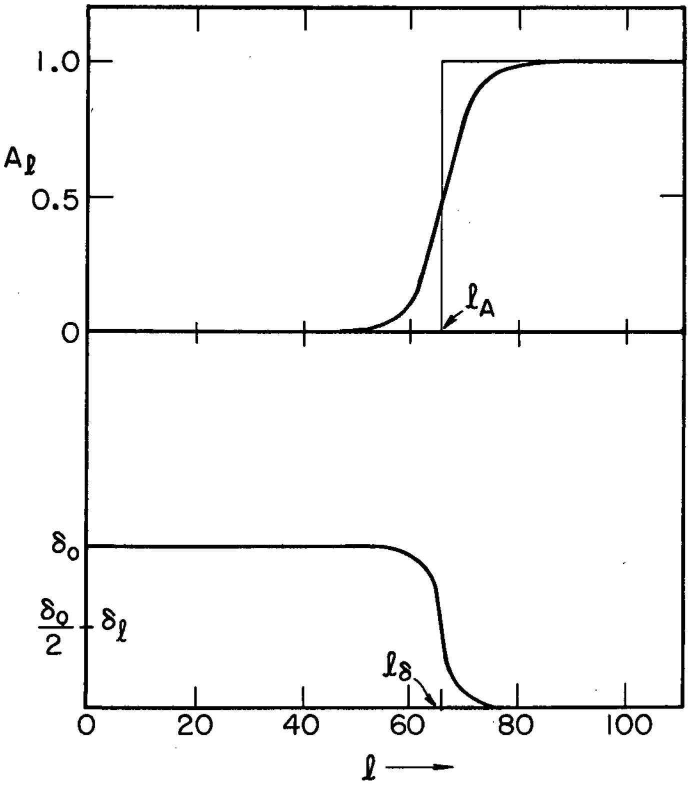

MU-23523

Fig. 4. The amplitude of the scattered partial waves and the real nuclear phase shift as a function of ℓ according to the McIntyre model.

The cross section then becomes

$$\frac{\sigma(\theta)}{\sigma_R(\theta)} = \left\{ \cos\left(n \ln \sin^2 \frac{1}{2}\theta\right) + \frac{\sin^2 \frac{1}{2}\theta}{n} \sum_{\ell=0}^{\infty} (2\ell+1) \right.$$

$$\left. [\sin 2(\sigma_\ell - \sigma_0) - A_\ell \sin 2(\sigma_\ell - \sigma_0 + \delta_\ell)] P_\ell(\cos\theta) \right\}^2$$

$$+ \left\{ \sin\left(n \ln \sin^2 \frac{1}{2}\theta\right) \right.$$

$$+ \frac{\sin^2 \frac{1}{2}\theta}{n} \sum_{\ell=0}^{\infty} (2\ell+1) [\cos 2(\sigma_\ell - \sigma_0)$$

$$\left. - A_\ell \cos 2(\sigma_\ell - \sigma_0 + \delta_\ell)] P_\ell(\cos\theta) \right\}^2 . \qquad (1.11)$$

The derivation is given in Appendix A. The calculation has to be performed for the whole range of angles and for ℓ's up to about 100. Since many angular distributions have to be calculated before a good fit is obtained, the actual calculation has been programmed for an IBM 704 computer (see Appendix B).

The range of the rounding of the amplitudes is controlled by $\Delta\ell_A$, and similarly $\Delta\ell_\delta$ controls the smoothness of the variations of δ_ℓ with ℓ ; δ_0 is the strength of the real nuclear phase shift. The ℓ_A and ℓ_δ compare with ℓ' of the Blair sharp-cutoff model.

Instead of the simple "one parameter" model, one now has a five-parameter model: ℓ_A, $\Delta\ell_A$, δ, ℓ_δ and $\Delta\ell_\delta$. One can try to reduce the number of parameters by keeping $\ell_A = \ell_\delta$ and $\Delta\ell_\delta = \Delta\ell_A$ (see Sec. IV). The variation of ℓ_A and ℓ_δ controls the number of oscillations in such manner that increasing ℓ_A and ℓ_δ increases the number of oscillations and moves the first maximum to smaller angles. As expected, $\Delta\ell_A$ and $\Delta\ell_\delta$ control the smoothness of the curve. Increasing $\Delta\ell_A$ and $\Delta\ell_\delta$ reduces the amplitudes of the oscillations and makes the dropoff steeper, but leaves the position of the maxima and minima unchanged. Increasing δ_0 increases the amplitudes of the oscillations (it lowers the minima and raises the maxima).

The influence of the parameters is not as clear cut as indicated above. A change of any one parameter will slightly affect all the features of the curve.

In the McIntyre model a surface region can be defined[16] (see Fig. 1). In the sharp-cutoff model ℓ' defines the interaction radius R; in the rounded-cutoff model a radius R + ΔR can be defined that will correspond to the $(\ell_A + \Delta\ell_A)$th partial wave, or to the diffuseness of the surface. From Eq. (1.8) we get

$$\frac{\hbar^2 (2\ell + 1)\Delta\ell}{2mR^2} = \left(2E - \frac{Z_1 Z_2 e^2}{R}\right) \frac{\Delta R}{R} \quad . \tag{1.12}$$

The surface region S = ΔR will be defined by taking for $\Delta\ell$ the range of ℓ over which the value of A_ℓ changes from 0.9 to 0.1 $(\Delta\ell = 4.4\Delta\ell_A)$.

C. Total Reaction Cross Sections

The general formula for the total reaction cross section is[17]

$$\sigma_R = \pi ƛ^2 \sum_{\ell=0}^{\infty} (2\ell + 1) \; (1 - |\eta_\ell|^2) \tag{1.13}$$

In the McIntyre model $|\eta_\ell|$ is given by A_ℓ , and the total reaction cross section becomes

$$\sigma_R = \pi ƛ^2 \sum_{\ell=0}^{\infty} (2\ell + 1) \; (1 - A_\ell^2) \; . \tag{1.14}$$

The McIntyre model has been applied to the elastic scattering of heavy ions,[18, 19] and very good agreement with experimental data was obtained. The McIntyre model suggests a great similarity with the optical model and in Sec. VI the two models are compared.

II. EXPERIMENTAL PROCEDURE

A. Linear Accelerator

The scattering experiments were done with C^{12} ions, accelerated in the heavy-ion linear accelerator (Hilac) at the Lawrence Radiation Laboratory (see Fig. 5). Partly ionized C^{12} ions are accelerated with a Cockcroft-Walton generator at a voltage of 425 kv and brought into a resonating rf cavity. A buncher serves to adjust their velocity so that the ions enter the prestripper cavity with the correct phase. In the prestripper cavity the ions are accelerated to 1 Mev per nucleon. At this point, the ions have a charge +2; the stripper, a jet of mercury vapor, strips two more electrons off the ions, and $C^{12(+4)}$ ions are subsequently accelerated in the poststripper cavity. Drift tubes at zero voltage are placed in the cavities to occupy the negative parts of the standing wave. The tubes get progressively shorter down the machine as the velocity of the ions increases. The velocity of different ions coming out of the linear accelerator is therefore the same, and corresponds to an energy of 10 Mev per nucleon for all particles. The field gradient has to be adjusted to acquire this correct velocity. Strong-focusing magnets are mounted inside the drift tubes to keep the particles close to the axis of the cavity. The beam pulse length is 2 msec, at 10 to 15 repetitions per sec. The Hilac has been described by Edward L. Hubbard and others.[20] After leaving the machine the ions are magnetically deflected and led into our scattering chamber.

B. Scattering Chamber

A 25-cm-diam scattering chamber was built for our experiment (see Fig. 6). The beam enters the chamber through two sets of collimators, whose size can be adapted to fulfill the requirements of the particular experiment. Collimators A and B actually collimate a parallel beam, while A' and B' prevent the beam particles that are scattered by the walls from reaching the target. The collimators are just thick enough to stop the beam particles in order to minimize the amount of slit scattering. A typical collimation would be A=B=3mm and A'=B'=3.5mm. The target is placed at the center of the chamber. After passing through the target the beam is stopped in a Faraday cup. The scattered particles leave the chamber through a 0.05-mm Mylar window.

With this arrangement it is possible to measure at angles from

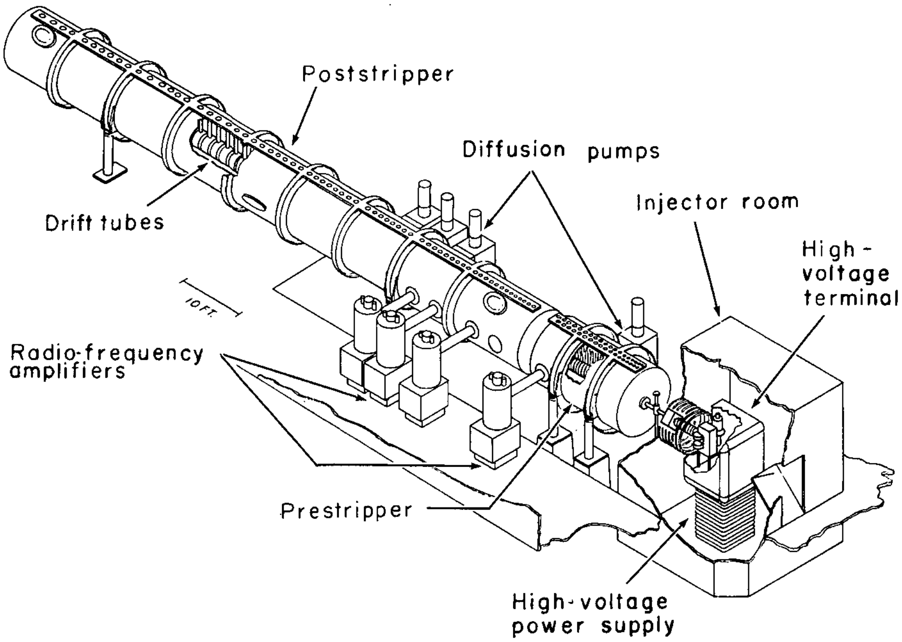

MU-22152-A

Fig. 5. Schematic view of the Hilac (from Ref. 15).

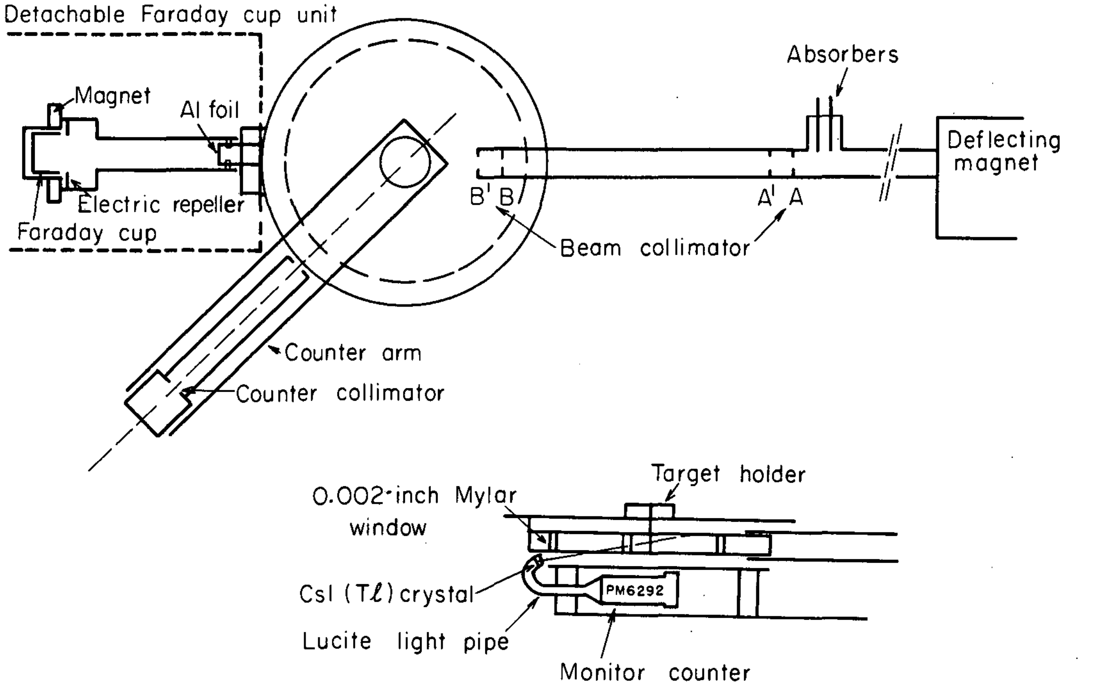

MU-23519

Fig. 6. Schematic top and side views of the scattering chamber and monitor.

15 to 170 deg. In many cases it is desirable to measure the scattering at angles smaller than 15 deg. For this purpose the Faraday cup unit can be detached from the chamber and replaced by a flange with a 0.025-mm aluminum window. The beam can then still be monitored with a counter, mounted at a fixed angle (14 deg). The monitor counter was used in all our experiments, with or without the Faraday cup.

C. Scintillation Counters

In the first phases of the experiment, the scattered particles were detected with a CsI (Tl) scintillation crystal mounted on a 6292 Dumont photomultiplier tube. The crystal was only 0.4 mm thick, sufficient to stop the C^{12} ions, but inefficient in detection of background particles such as neutrons and γ rays formed in the accelerator and collimators. Using a standard CsI crystal and photomultiplier tube, no better than an energy resolution of 6% could be obtained. Resolution was improved by experimenting with the preparation of the CsI crystal. The crystals were cut with a jeweler's blade from a 1.25-cm-diam cylinder and polished with fine carborundum sandpaper wetted with alcohol.

The crystals were tested with an α source. Subsequently, one of the sides of the crystal was water polished. However, water polishing both sides of the crystal gave the best results.

The resolution obtained with the same crystal changes by as much as 2 or 3% between different 6292 photomultipliers. Fifteen 6292 photomultipliers were tested and the best one selected. The crystals were mounted on the face of the photomultiplier with Dow-Corning silicone oil of 10^6 cst. Resolution depends very critically on the amount of grease used. The grease was heated on the face of the photomultiplier and was allowed to flow on the edges of the crystal (see Fig. 7-A) in order to facilitate the collection of light leaving the crystal at the edges, which may be a large fraction of the light output if a very thin crystal is used. Two counters were made with an energy resolution of 1.4% for 100-Mev C^{12} ions.

The light collection could not be improved appreciably by using a light pipe (see Fig. 7-B) to spread the light uniformly over the face of the photomultiplier. The performance of the various photomultipliers was now nearly the same for all the tubes, but not as good as if one were to select a good one and use only part of its face, without the light pipe. This indicates that the over-all efficiency is the same for all tubes, but that in some cases to use only a small part of the face is advantageous.

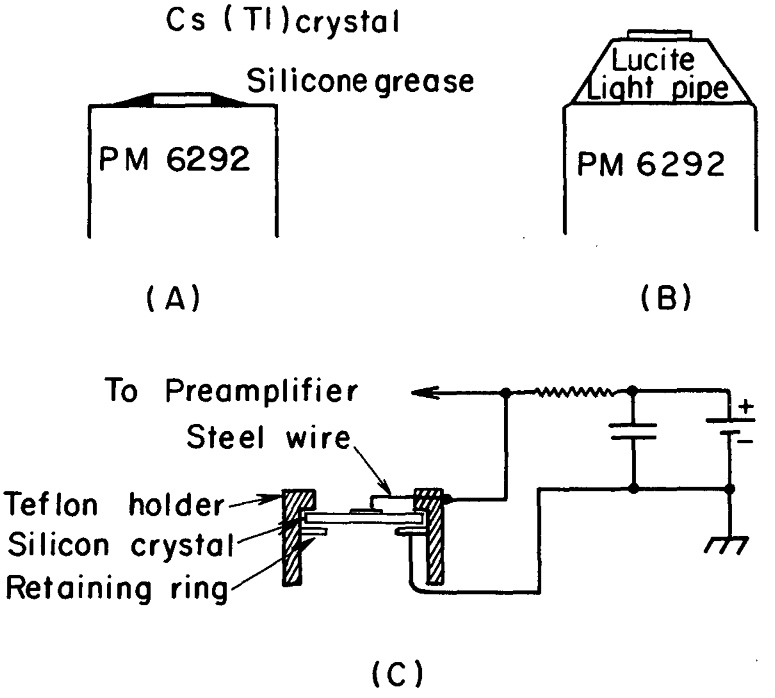

MU−23527

Fig. 7. (A) Mounting of CsI crystal on photomultiplier.
(B) Mounting of thin CsI crystal via lightpipe.
(C) Mounting of semiconductor crystal.

The response of CsI for several heavy ions as a function of energy is given in Fig. 8 (and see Ref. 21). It is quite nonlinear at low energies but becomes linear above about 70 Mev. The experiments were done in the linear region, where we can write E = kV + 30 Mev. The measured pulse-height resolution $\Delta V/V$ transforms therefore to energy resolution in the following way: $\Delta E/E = (\Delta V/V)\,(1-30/E)$. At about 100 Mev $\Delta V/V$ is approximately 2% and $\Delta E/E = 1.4\%$.

A closer study of Fig. 8 suggests that the light output of different heavy ions is approximately the same for the same velocity (see Fig. 9). Consequently, the pulse height from the CsI crystal will be the same for a C^{12} ion of 100 Mev and a C^{11} ion of 90 Mev, or a N^{13} ion of 110 Mev, and in the energy spectrum one cannot separate these particles from the elastically scattered C^{12} ions.

D. Solid-State Radiation Detector

Investigations at the Lawrence Radiation Laboratory showed that the response of solid-state radiation detectors is linear with energy, [22] independent of the type of particle detected (see Fig. 10). (There is some evidence of nonlinearity of about 5% for fission fragments.[23]) The CsI counter was therefore replaced by a semiconductor crystal, which had the additional advantage of giving a slightly better energy resolution.

The detector was made by diffusing phosphorus in a p-type silicon wafer, thereby creating n material at the surface.[24] At the p-n junction, a "depletion layer" is formed, where only a few charge carriers are present. An ionizing particle entering this region gives rise to a current flow. The thickness of the depletion layer (the effective thickness of the detector) is a few microns.[25] It can be increased by applying a reverse bias voltage (positive on the n side):

$$W = 1.05 \sqrt{\frac{\epsilon(V_0 + V_b)}{2\pi e N}} \times 10^{-6}\ \text{cm} ,$$

where W is the thickness of the depletion layer

ϵ is the dielectric constant of the silicon,

V_0 is the potential created at the junction when no external

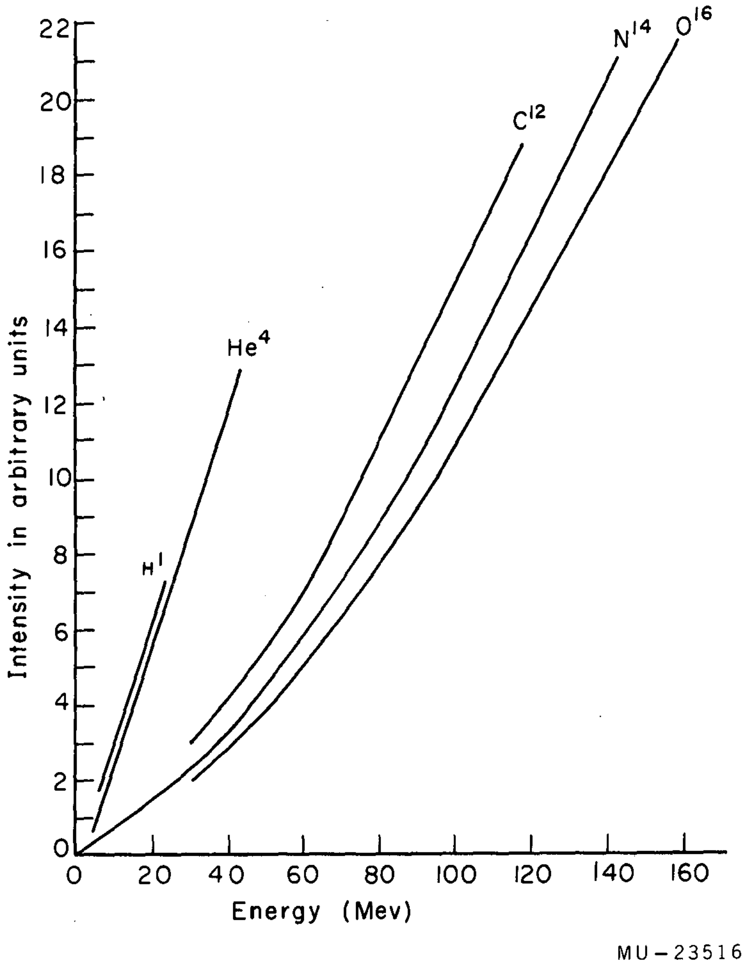

Fig. 8. Response of CsI as a function of energy (from Ref. 16).

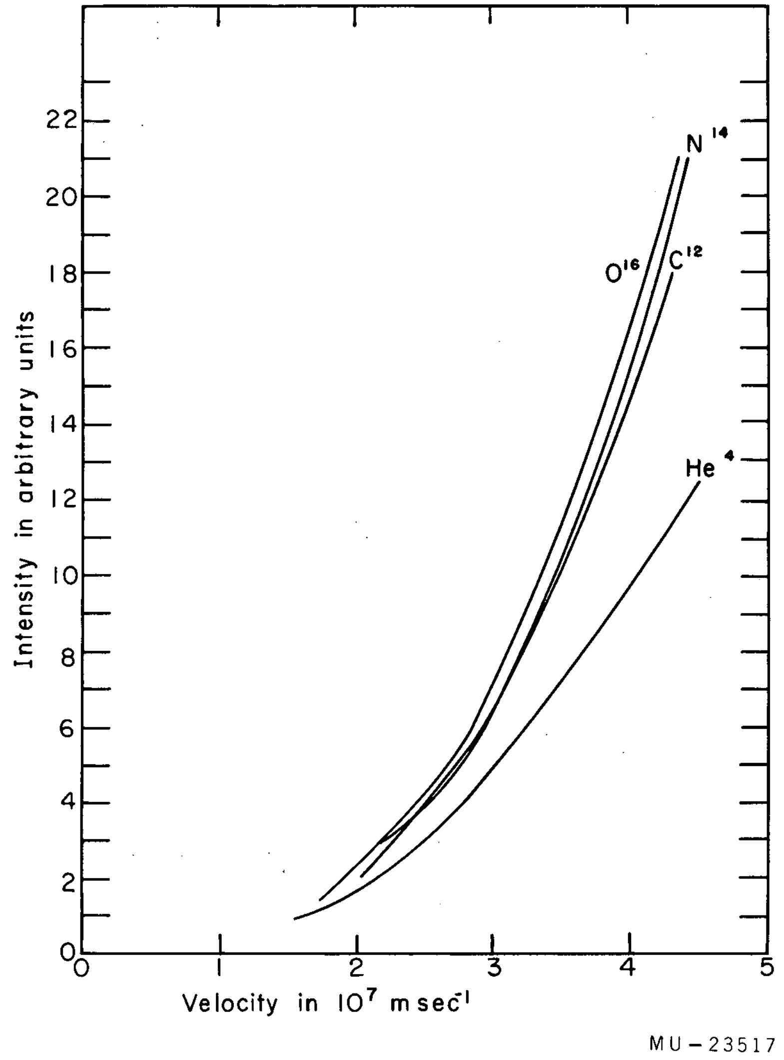

Fig. 9. Response of CsI as a function of velocity.

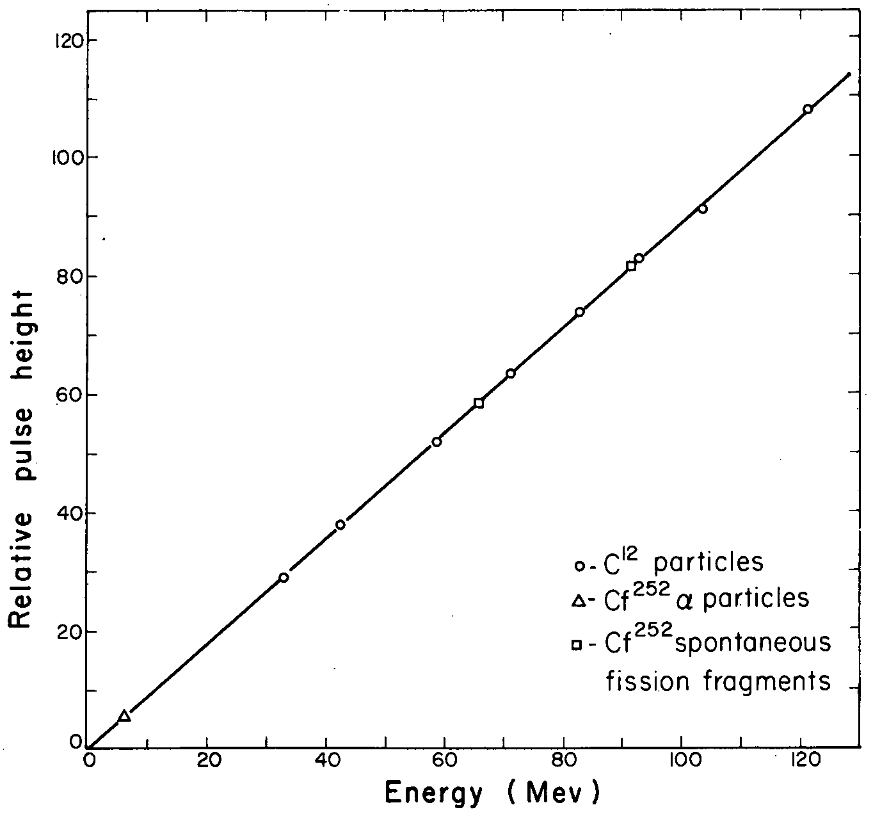

MU-19582

Fig. 10. Response of the solid-state radiation detector to different particles at various energies (from Ref. 17).

voltage is applied,

V_b is the bias voltage,

N is the concentration of the acceptor atoms initially present in Si,

e is the electronic charge.

The potential that can be applied is limited by the resistivity of the material, and by leakage currents. For 100-Mev C^{12} ions a thickness of 0.3 mm is necessary to stop the particles in the depletion layer. The necessary bias voltage was therefore 100 v, since the resistivity of the silicon was 4000 ohm-cm. The counter assembly is shown in Fig. 7-C. The crystal was mounted in a Teflon holder. The signal was taken from the n side of the crystal. Aluminum was diffused on the p side and a wire soldered to it to make electrical contact. A spring wire made a point contact on the front of the crystal.

E. Electronic Equipment

The pulses from the silicon counter were fed into a low-noise preamplifier[25] and subsequently brought into a double-line linear pulse amplifier[26] through a 30-m-long cable. The pulses were recorded in a scaler and the energy spectra measured with a Penco 100-channel pulse-height analyzer. Since the Hilac is a pulsed machine with a duty cycle of 2 to 3%, the dead time of the pulse-height analyzer becomes an important factor. During each 2-msec beam burst, the intensity had to be sufficiently low so that the dead time of the analyzer should not cause any losses in counts. The Penco has a dead time of 28 + 2× (channel number) μsec; however, a second pulse arriving 7.5 μsec after the first is put into temporary storage and is not lost. It is advantageous to store the elastic peak in the energy spectrum in the low channels, in order to minimize the dead time. This can easily be accomplished by turning up the threshold of the analyzer, which changes the voltage acceptance range of the analyzer and still does not distort the Gaussian shape of the peak. Typically, the elastic peak was put in the neighborhood of channel 30, resulting in a dead time of about 60 μsec, and roughly two pulses per 100 μsec should be acceptable. The maximum counting rate is therefore 600 per sec. compared to 20,000 per sec for continuous accelerator. If the pulses were uniformly distributed in time during a beam burst, the adopted counting rate would not cause any losses of counts; since this was not the case a correction has to be made. Typical energy spectra are shown in Fig. 11.

F. Monitor

The monitor counter is shown in Fig. 6. The light pipe was made of lucite. The CsI crystal was 5 mm in diameter and 0.8 mm thick. Bigg's cement was used to glue the crystal to the light pipe and the light pipe to the photomultiplier. An energy resolution of 3% was obtained even though the light pipe had a strong curvature and a diameter of 5 mm. The collimators in front of the monitor could be changed during runs, so that the monitor scalers would not become overloaded when the beam was increased.

G. Targets

The nuclear radius as derived from the scattering experiments is strongly dependent upon the energy of the projectiles at the instant of scattering. This energy is most easily determined if the energy loss of the particles in the target is negligible. Using Eq. (1.3), and remembering that we want to determine R with a precision of 1%, we find that the energy loss has to be less than 1 Mev for 120-Mev C^{12} ions. For a large energy loss, moreover, the details in the structure of the angular distribution are washed out, due to averaging over a large energy region. Targets of 1 mg/cm^2 thickness were therefore required. The preparation of such thin targets is especially difficult if no backing material can be used, as was the case here, because any backing material would contribute appreciably to the number of elastically scattered particles.

Self-supporting Ta and Fe targets were made by rolling films down to the desired thickness with steel rolls. Ag^{107} and In films were made by vacuum deposition out of a tungsten crucible onto a glass plate.[27] The films were stripped off the glass and mounted on brass rings. Ni films 1.2 μm thick were commercially available.[28]

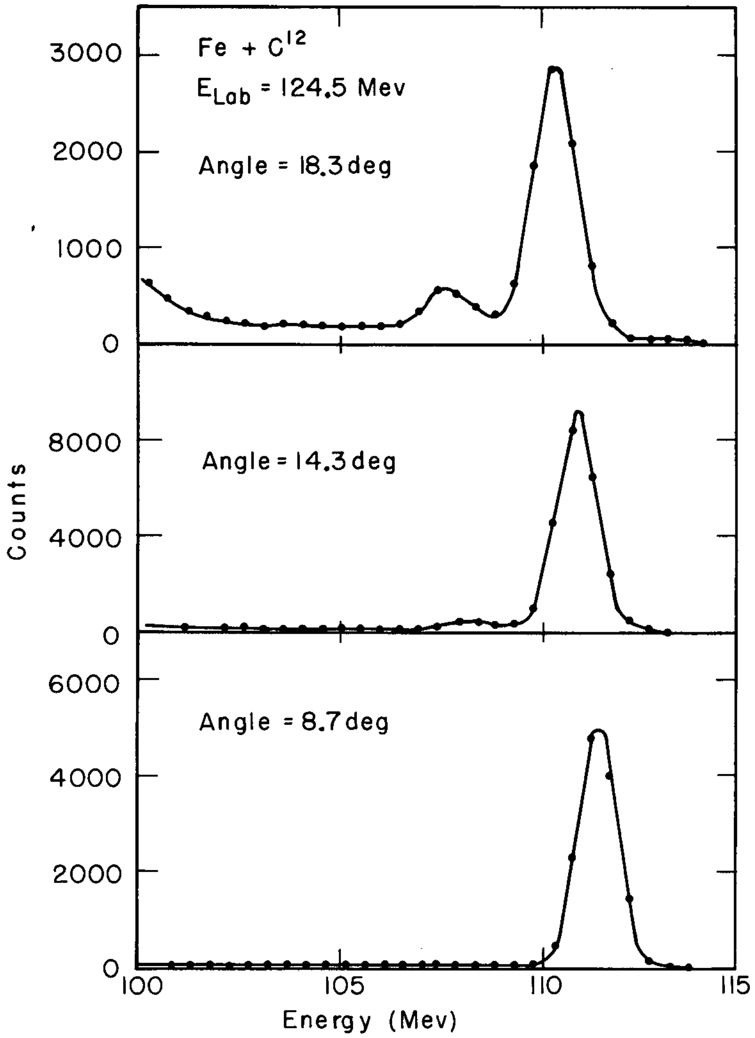

MU-23524

Fig. 11. Typical energy spectra taken with the CsI scintillation counter.

H. Gas Targets

The scattering chamber is easily adapted to the use of gas targets. A 2.5-μm nickel foil at the left of the collimator B' (see Fig. 6) and a 0.025-mm aluminum foil separate the accelerator and Faraday cup vacuum from the scattering chamber. The whole scattering chamber is filled with the target gas. The efficiency for scattering into the detector at an angle θ is, therefore, a rather complicated function of the parameters defining the geometry of the arrangement and is explained in Fig. 12. If we combine them in a quantity $G = 2\pi w r^2/ab$, the cross section for scattering at an angle θ is obtained from the number N_i of incident particles, the N(θ) of detected particles, and the number N_V of target nuclei per unit of volume:

$$d\sigma(\theta)/d\Omega = N(\theta) \sin\theta \,/\, N_i N_V G$$

(see Ref. 29, 30. 31).

Evidently the effective thickness can become very large at small angles. This effect can be compensated for by lowering the gas pressure.

I. Precision and Corrections

The counters were moved manually and the angular settings could be reproduced to within 0.1 degree.

If the beam axis does not coincide with the chamber axis, a large error is introduced in the scattering angle, especially since measurements were taken at both sides of the chamber. For gas targets, this also introduces an error in the effective target thickness.

If ϕ is the angle between the beam axis and the chamber axis, with our dimensions, at a scattering angle $\theta = 8$ deg, $\phi = 1$ deg would introduce an error of 13% in the cross section for a gas target. An optical alignment system was therefore used every time both collimator sets were changed, to ascertain that the beam axis and chamber axis coincided. During each run the alignment was further checked by measuring the cross section at 6, 7, and 8 deg on both sides of the chamber. The checks proved that deviations were never larger than 0.1 deg.

An angular spread is caused by the finite aperture of the

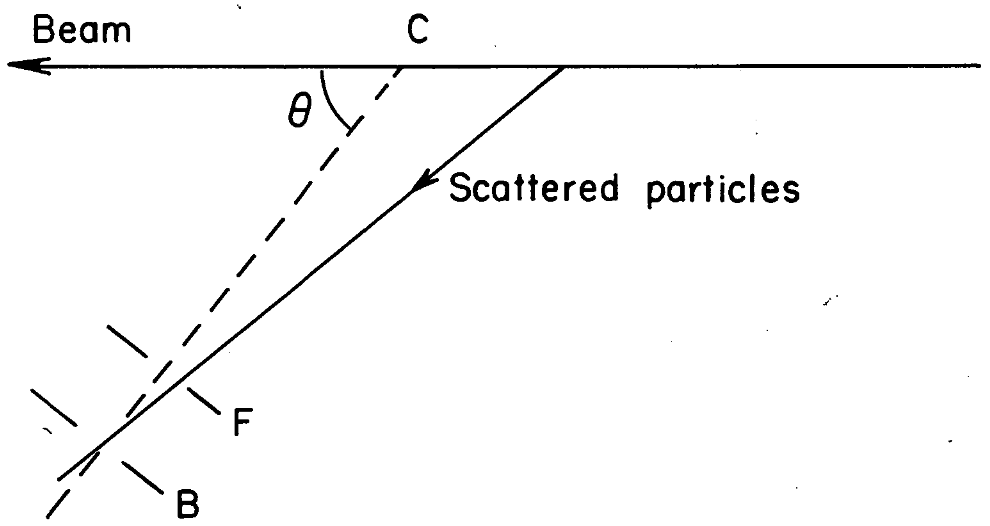

MU-23580

Fig. 12. The gas target geometry in the horizontal plane.

counter collimator and the size of the beam spot on the target. Assuming that the beam density is constant over the beam area (which is probably very nearly correct, since the collimator selects only a small part of the center of the beam), the intensity distribution for the beam spot-counter system can be calculated by "folding" the two separate distributions (see Fig. 13).

The beam spot on the target is a circle with a 1.6-mm radius. The detector is a circle with the same radius. For an infinitely small slit at the detector, the angular spread due to the size of the beam spot can be represented by $g(t)=2\sqrt{1-t^2}$, where $t = 0$ corresponds to the nominal scattering angle θ_0 and the angular spread $t=t_1$ corresponds to the angle $\theta_0 + \Delta\theta$ through the relationship $\Delta\theta = \arctan t_1/d$ (d being the distance between the target and the detector). Analogously, the spread due to the size of the detector is $f(y) = 2\sqrt{1-y^2}$. The "folding" of these two distributions is depicted in the insert of Fig. 13; the resulting distribution is given by $I(t) = \int_{t-1}^{1} g(y-t)\ f(y)\ dy$, and is plotted in Fig. 13. Here $t = 2$ corresponds to $\Delta\theta = 0.5$ degree. I(t) turns out to be nearly identical with a Gaussian curve; the standard deviation is therefore a good measure for the angular spread of the system.

J. Multiple Scattering

Multiple scattering at the chamber window adds to the spread calculated above. The root-mean-square angle for this multiple scattering is 0.5 deg for a typical case in our experiments.[32, 33] Since the distribution in Fig. 13 and the multiple scattering distribution are both nearly Gaussian, the spreads can be added quadratically:

$$\sigma = \sqrt{\sigma_1^2 + \sigma_2^2}$$

No correction is necessary for the number of particles scattered out of the solid angle due to multiple scattering in the windows; in sufficient approximation, the number of particles scattered out will be equal to the number of particles scattered into the solid angle from outside.

The contribution to the angular spread due to multiple scattering in the target can be neglected, but it sets a lower limit of approx-

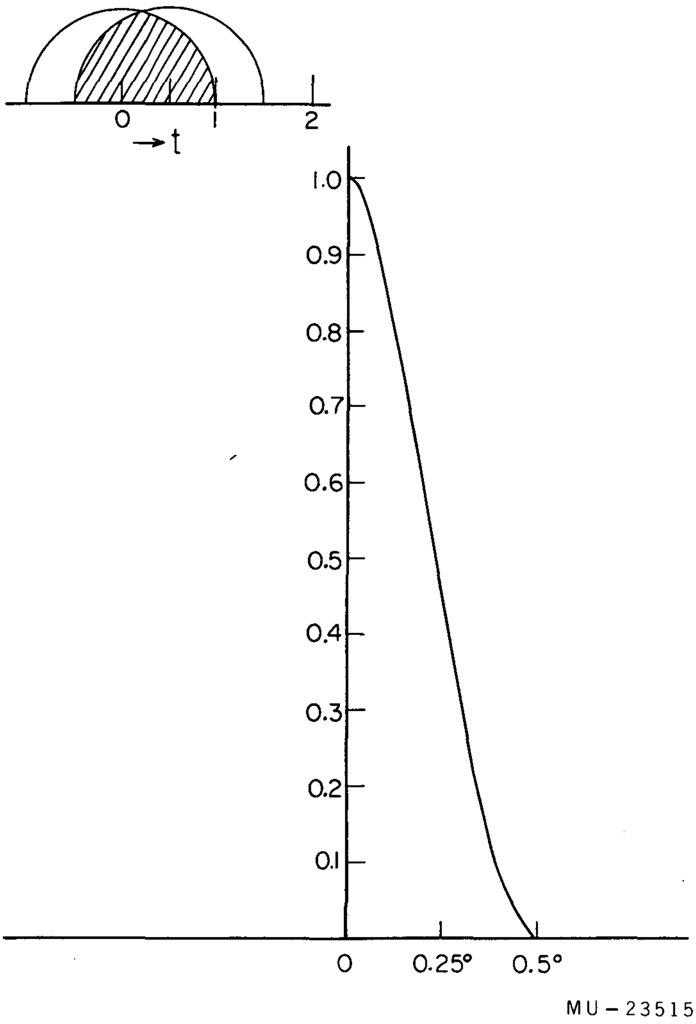

Fig. 13. Distribution of intensity over the angle, calculated by "folding" the two distributions in the insert.

imately 5 deg for the angle where the elastic scattering can be meas-used. At small angles, a second-order correction has to be made allowing for the large change in cross section over the angular spread.[30, 31]

K. Cross Sections

In most of the experiments the differential cross sections have been divided by the Coulomb cross section and then normalized to unity by drawing a straight line through the average of the points close to zero degrees. This is justified by the fact that the cross sections oscillate slightly around the pure Coulomb scattering cross section for small-angle scattering, as explained qualitatively in Sec. 1. The error introduced this way is at most 2%, and even less for very heavy targets. In principle, cross sections could be measured absolutely by measuring accurately the charge collected in the Faraday cup, the target thickness, and the counter target distance. Unfortunately, however, the target thickness cannot be obtained with a better precision than about 5%. The target can be weighed very accurately, but a large error is made in the measurement of the area where the beam hits the target. The foils were not sufficiently uniform that the weighing of the whole foil was of any use. In addition, the beam charge collected cannot be measured more accurately than 1% because of instability of the electrometer, the unknown loss of secondarily emitted electrons from the Faraday cup, and the capture of knock-out electrons from the target. The above method of normalization was therefore chosen to represent the data, although in some cases both methods were used and found to agree within the expected errors.

For the light targets Fe and A, the above normalization could not be applied, since the region of oscillations around Rutherford scattering could not be reached. Consequently, larger errors have to be assigned to the absolute cross sections in these cases; but the errors of points in the angular distribution relative to each other are the same as in the other cases, i.e., the angular distribution curve as a whole can be moved up or down by several percent, but not the points separately.

III. EXPERIMENTAL RESULTS

The experimentally measured angular distributions are listed in Tables I, III, V, VII, IX and XI, and are also plotted in Fig. 14.

Column 1 gives the center-of-mass angle; the spread is ±0.7 deg.

Column 2 gives the measured cross section divided by the Rutherford cross section, normalized as already discussed. The cross sections are corrected for all the effects listed in the preceding section.

In column 3, the error includes the statistical error in the number of counts and the uncertainty in separating the elastic peak in the energy spectrum from the inelastic peak (important only for large angles); $\lambdabar$ is the de Broglie wave length, and n is the classical parameter ($n = Z_1 Z_2 e^2/\hbar v$).

The analyses of experimental data with the McIntyre model, using formula (11), are given in Tables II, IV, VI, VIII and X. The first five columns give the parameters of the model.

Column 6 is $\Delta = \Sigma \mid (\text{calculated-measured})/\text{measured} \mid \times 100$, summed over all calculated angles. A value near the sum of statistical errors for this quantity, indicates a good fit between experiment and theory.

Column 7 gives the total reaction cross section calculated with Eq. (1.13), where the summation is performed up to ℓ, such that $A(\ell) \geqslant 0.9999$.

The sets of parameters listed all give good agreement with the experimental data. They are the results of an extensive search for best fits. The chance that good fits could be obtained for very different values of these parameters is exceedingly remote.

The criterion for a good fit was that the following features, in decreasing order of importance, should be reproduced very well:

(a) the sharp break from Rutherford scattering,
(b) the initial rise above Rutherford scattering,
(c) the exact slope of the steep fall-off, and
(d) the oscillations around Rutherford scattering.

The limits of the parameters that still give a good fit to the data are best presented in a table, because a two-dimensional graph of a five-dimensional space is not easy to read.

In the first group of fits, $\ell_A = \ell_\delta$, and $\Delta\ell_A \neq \Delta\ell_\delta$;

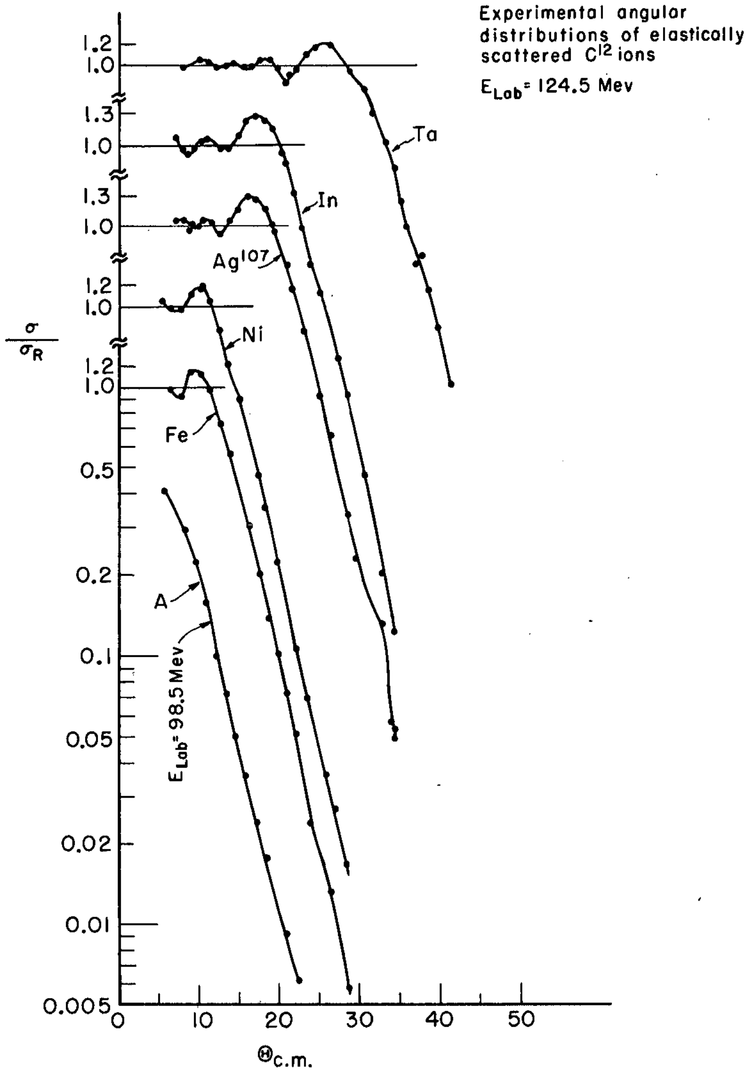

MU-23520

Fig. 14. Experimental angular distribution of C^{12} ions elastically scattered from A, Fe, Ni, Ag^{107}, In, and Ta.

In the second group of fits, $\ell_A = \ell_\delta$, and $\Delta\ell_A \neq \Delta\ell_\delta$

In the third group, all parameters were changed independently. One fit in each group, marked *, has been plotted in a graph together with the experimental points (see Figs. 15 through 22). The interaction radius is calculated by substituting ℓ_A for ℓ' in Eq. (1.7). The error in the radius arises from the fact that the scattering can occur at an energy E_0 ± 1 Mev. The surface parameter S is calculated by using Eq. (1.12), substituting for $\Delta\ell$ 4.4 times the maximum and minimum values values of the $\Delta\ell_A$'s in the table.

A. Ta + C^{12}

The results for Ta + C^{12} are summed up in Tables I and II, and Figs. 15 and 16.

For ℓ_A = 65: the interaction radius R $= (11.51 \pm 0.07) \times 10^{-13}$ cm.

For ℓ_A = 66: the interaction radius R $= (11.63 \pm 0.07) \times 10^{-13}$ cm.

For ℓ_A = 65: the surface region S is $1.58 < S < 2.02 \times 10^{-13}$ cm.

For ℓ_A = 66: the surface region S is $1.28 < S < 1.63 \times 10^{-13}$ cm.

The initial rise above Rutherford scattering is 20%.

The fits with the McIntyre model are very good in this case.

The small oscillations of σ/σ_R around 1 are very well reproduced.

Table I

Experimental results: Ta + C^{12}

$\theta_{c.m.}$ (deg)	$\left(\frac{d\sigma}{d\Omega}\right) / \left(\frac{d\sigma}{d\Omega}\right)_R$	Error (%)	$\theta_{c.m.}$ (deg)	$\left(\frac{d\sigma}{d\Omega}\right) / \left(\frac{d\sigma}{d\Omega}\right)_R$	Error (%)
7.9	0.980	1	23.2	1.088	1
9.0	1.003	1	24.2	1.137	1
10.2	1.036	1	26.3	1.184	1
11.2	1.007	1	28.5	0.934	1
12.2	0.975	1	30.6	0.811	1
13.3	0.985	1	31.6	0.668	1
14.4	1.013	1	33.3	0.512	3
15.5	0.988	1	34.3	0.414	1
16.5	0.985	1	34.9	0.311	1
17.6	1.041	1	35.8	0.249	1
18.7	1.044	1	37.0	0.181	1
19.7	0.973	1	37.6	0.199	1
20.8	0.859	1	38.7	0.147	2
21.0	0.923	1	39.6	0.106	3
22.1	0.957	1	41.2	0.0645	3

Target thickness = (2.2±0.2) mg/cm^2;

λ = 0.127 f; $E_{c.m.}$ = 114.9 Mev n = 21.59.

Table II

Theoretical analysis: Ta + C^{12}

ℓ_A	ℓ_δ	$\Delta\ell_A$	$\Delta\ell_\delta$	δ	Δ^2	σ_{Reaction} (b)
*65	65	3.0	3.0	0.4	89	2.40
65	65	3.8	1.0-3.0	0.3	116-97	2.46
*65	65	3.6	2.0-3.0	0.3	102-92	2.44
65	65	3.2	1.0-3.0	0.4	102-95	2.41
65	65	3.2	3.0	0.3	122	2.41
65	65	3.0	1.0-2.0	0.4	121-93	2.40
*65	66	3.3	2.0-3.2	0.3	81-89	2.42
65	66	3.0	2.0-2.9	0.3	102-114	2.40
*66	66	2.7	2.7	0.3	109	2.44
66	66	2.4	2.4	0.3	146	2.42
*66	66	3.0	2.0-3.5	0.3	90-119	2.46
66	66	2.8	2.0-2.5	0.3	100-103	2.45
66	66	2.6	2.0-3.5	0.3	132-126	2.43
66	65	2.8	2.0-3.5	0.3	131-118	2.45
66	65	2.8	2.5	0.4	107	2.45
*66	65	3.0	2.0-3.5	0.3	109-100	2.46
66	65	3.0	2.0	0.4	100	2.46

---

*Plotted in graph.

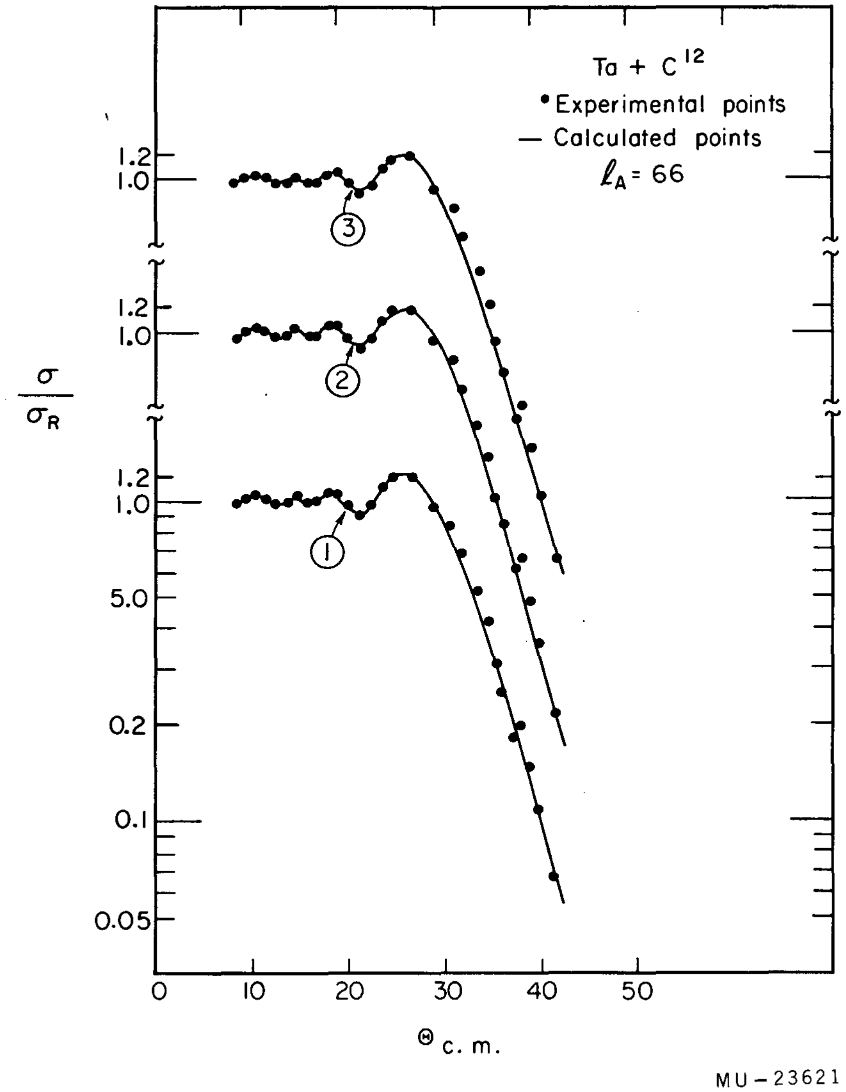

Fig. 15. Angular distributions of C^{12} ions elastically scattered from Ta at $E_{\text{lab}} = 124.5$ Mev. The dots are the measured cross sections and the solid line is the calculated cross section with the following McIntyre model parameters.

	ℓ_A	$\Delta\ell_A$	δ	ℓ_δ	$\Delta\ell_\delta$	Δ
(1)	66	2.7	0.3	66	2.7	109
(2)	66	3.0	0.3	66	2.0	90
(3)	66	3.0	0.3	65	2.5	101

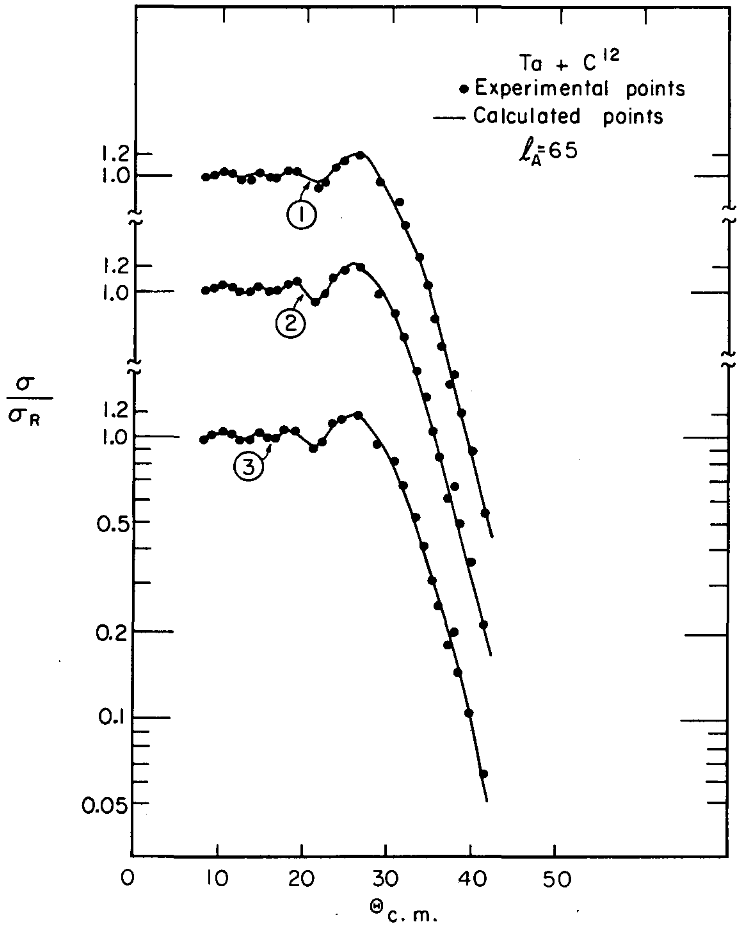

MU-23622

Fig. 16. Angular distribution of C^{12} ions elastically scattered from Ta at E_{lab} = 124.5 Mev. The dots are the measured cross sections and the solid line is the calculated cross section with the following McIntyre model parameters.

	ℓ_A	$\Delta\ell_A$	δ	ℓ_δ	$\Delta\ell_\delta$	Δ
(1)	65	3.6	0.3	65	3.0	92
(2)	65	3.0	0.4	65	3.0	89
(3)	65	3.3	0.3	66	2.6	82

B. In + C^{12}

The results for In + C^{12} are summed up in Tables III and IV, and Figs. 17 and 18.

For $\ell_A = 61$: the interaction radius R $= (10.24 \pm 0.06) \times 10^{-13}$ cm.

For $\ell_A = 62$: the interaction radius R $= (10.36 \pm 0.06) \times 10^{-13}$ cm.

For $\ell_A = 61$: the surface parameter S is $1.01 < S < 1.36 \times 10^{-13}$ cm.

For $\ell_A = 62$: the surface parameter S is $1.14 < S < 1.36 \times 10^{-13}$ cm.

The initial rise above Rutherford scattering is about 30%.

The fits with the McIntyre model are very good, and the small oscillations around $\sigma/\sigma_R = 1$ are very well reproduced.

Due to the large rise, the value of δ_0 is quite large in this case.

Table III

Experimental result: In + C^{12}

$\theta_{c.m.}$ (deg)	$\left(\frac{d\sigma}{d\Omega}\right) / \left(\frac{d\sigma}{d\Omega}\right)_R$	Error (%)	$\theta_{c.m.}$ (deg)	$\left(\frac{d\sigma}{d\ell}\right) / \left(\frac{d\sigma}{d\ell}\right)_R$	Error (%)
7.1	1.069	1	19.2	1.113	1
8.2	0.960	1	20.3	0.937	1
8.4	0.933	1	20.8	0.855	1
9.3	0.964	1	21.7	0.663	1
9.5	0.981	1	22.8	0.469	1
10.4	1.023	1	23.9	0.359	1
11.6	1.030	1	25.0	0.282	1
12.7	0.989	1	27.2	0.155	1.5
13.8	0.983	1	28.3	0.117	3
14.8	1.085	1	30.5	0.589	3
15.9	1.245	1	32.7	0.0258	1.5
17.0	1.290	1	34.4	0.0152	4
18.1	1.231	1			

Target thickness = 1.5 ± 0.2 mg/cm^2;

ƛ = 0.132 f; $E_{c.m.}$ = 110.9 Mev; n = 14.49.

Table IV

Theoretical analysis: In + C^{12}

ℓ_A	ℓ_δ	$\Delta\ell_A$	ℓ_δ	δ	Δ	$\sigma_{Reaction}$ (b)
61	61	2.0	2.0	1.1	276	2.20
61	61	2.1	2.0	1.0	255	2.21
*61	61	2.2	2.2	0.9-1.0	253-251	2.22
61	61	2.4	2.4	1.0	184	2.23
61	61	2.0	2.8	1.0	173	2.20
61	61	2.2	2.4	1.0	163	2.22
*61	61	2.4	2.8-3.6	0.8	173-162	2.23
61	62	1.8	3.0	0.8	198	2.19
61	62	2.0	3.0	0.7	238	2.20
*61	62	2.0	2.5	0.8	155	2.20
61	62	2.0	2.0	0.9	185	2.20
61	62	2.2	2.0	0.8	164	2.22
61	62	2.2	3.0	0.7	176	2.22
62	62	2.0	2.0	0.9	284	2.27
*62	62	2.2	2.2	0.8	242	2.29
62	62	2.2	2.8	0.8	185	2.29
62	62	2.4	2.4-2.8	0.8	167-180	2.30
*62	61	2.2	2.5-3.0	1.0	251-208	2.29
*62	63	2.3	2.5	0.6	200	2.29
62	63	2.3	1.5	0.7	216	2.29

*Plotted in graph.

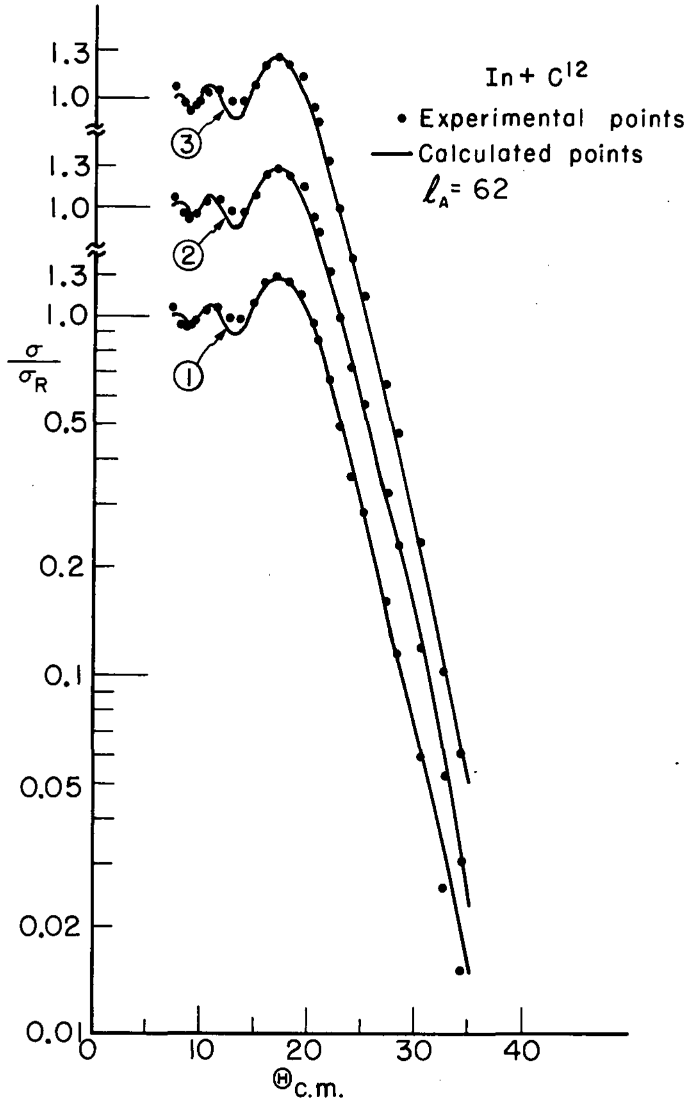

MU-23619

Fig. 17. Angular distribution of C^{12} ions elastically scattered from In at E_{lab} = 124.5 Mev. The dots are the measured cross sections and the solid line is the calculated cross section with the following McIntyre model parameters.

	ℓ_A	$\Delta\ell_A$	δ	ℓ_δ	$\Delta\ell_\delta$	Δ
(1)	62	2.2	0.8	62	2.2	242
(2)	62	2.3	0.6	63	2.5	200
(3)	62	2.2	1.0	61	3.0	208

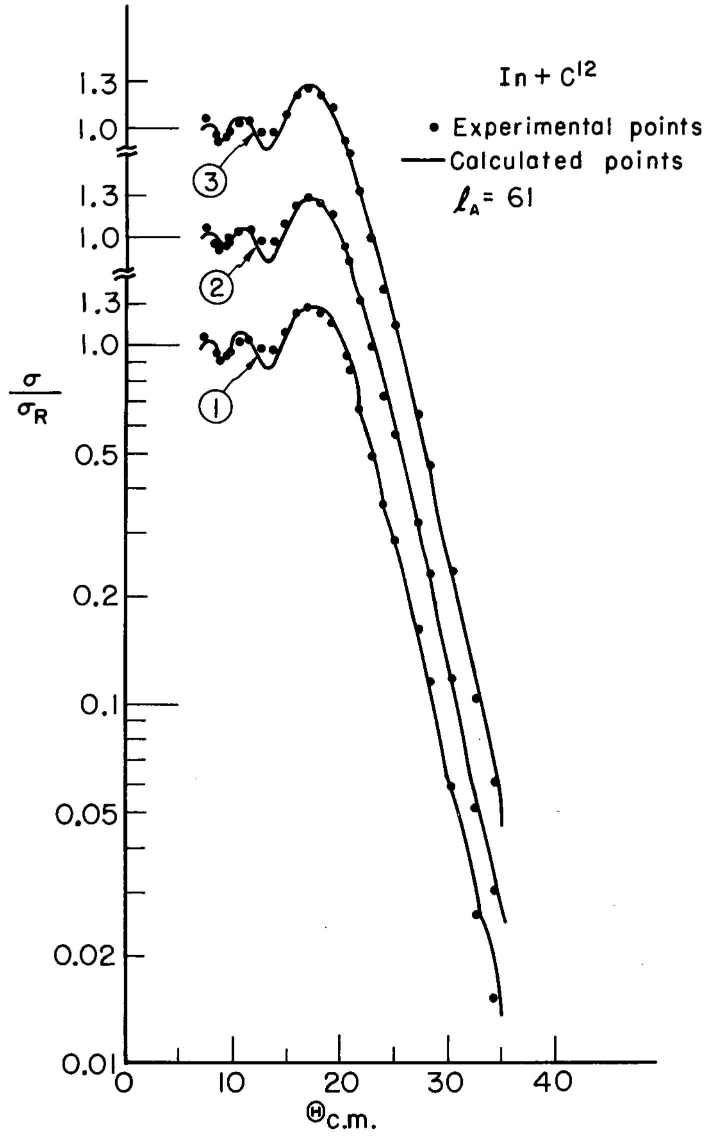

MU-23618

Fig. 18. Angular distribution of C^{12} ions elastically scattered from In at E_{lab} = 124.5 Mev. The dots are the measured cross sections and the solid line is the calculated cross section with the following McIntyre model parameters.

	ℓ_A	$\Delta\ell_A$	δ	ℓ_δ	$\Delta\ell_\delta$	Δ
(1)	61	2.2	1.0	61	2.2	203
(2)	61	2.4	0.8	61	3.2	153
(3)	61	2.0	0.8	62	2.5	155

C. $Ag^{107} + C^{12}$

The results for $Ag^{107} + C^{12}$ are summed up in Tables V and VI, and Figs. 19 and 20.

For $\ell_A = 60$: the interaction radius R $= (10.09 \pm 0.06) \times 10^{-13}$ cm.

For $\ell_A = 61$: the interaction radius R $= (10.22 \pm 0.06) \times 10^{-13}$ cm.

For $\ell_A = 60$: the surface parameter S is $1.14 < S < 1.58 \times 10^{-13}$ cm.

For $\ell_A = 61$: the surface parameter S is $1.14 < S < 1.58 \times 10^{-13}$ cm.

The initial rise above Rutherford scattering is about 27%.

Table V

Experimental results: $Ag^{107} + C^{12}$

$\theta_{c.m.}$ (deg)	$\left(\frac{d\sigma}{d\Omega}\right) / \left(\frac{d\sigma}{d\Omega}\right)_R$	Error (%)	$\theta_{c.m.}$ (deg)	$\left(\frac{d\sigma}{d\Omega}\right) / \left(\frac{d\sigma}{d\Omega}\right)_R$	Error (%)
6.9	1.050	1	19.2	0.948	1
8.0	1.054	1	20.3	0.806	1
8.6	0.969	1	20.7	0.738	1
9.1	1.033	1	21.6	0.580	1
9.7	0.996	1	21.9	0.530	1
10.4	1.056	1	23.0	0.409	1
11.5	1.031	1	25.0	0.234	2
12.6	0.931	1	26.3	0.167	1
13.7	1.027	1	27.4	0.118	1.5
14.8	1.151	1	28.5	0.0842	1.5
16.0	1.279	1	29.6	0.0584	1.5
17.0	1.248	1	32.9	0.0331	2
18.2	1.177	1	34.0	0.0142	3
19.0	1.014	1	34.4	0.0133	1.5

Target thickness = 1.8 ± 0.1 mg/cm^2;

$\bar{\lambda}$ = 0.133 f; $E_{c.m.}$ = 110.1 Mev; n = 13.90.

Table VI

Theoretical analysis: $Ag^{107} + C^{12}$

ℓ_A	ℓ_δ	$\Delta\ell_A$	$\Delta\ell_\delta$	δ	Δ	$\sigma_{Reaction}$ (b)
*60	60	2.5	2.5	0.8-0.9	166-190	2.20
60	60	2.7	2.7	0.8	194	2.22
60	60	2.8	2.0	0.9	174	2.22
60	60	2.6	2.0	0.9-1.0	193-184	2.21
60	60	2.6	2.5	0.8	177	2.21
*60	60	2.4	2.5	0.9	151	2.19
60	60	2.4	3.0	0.8	156	2.19
60	60	2.0	3.0	0.9	160	2.16
60	60	2.0	2.5	1.0	163	2.16
60	61	2.6	3.0	0.6	196	2.21
60	61	2.4	2.5-3.0	0.7	172-155	2.19
*60	61	2.2	2.5-3.0	0.7	197-162	2.18
60	61	2.0	2.5	0.8	148	2.16
61	61	3.0	3.0	0.6	188	2.31
*61	61	2.5	2.5	0.6-0.8	153-167	2.27
61	61	2.0	2.0	1.0	225	2.23
61	61	2.8	2.0	0.8	154	2.29
61	61	2.8	2.8-3.0	0.6	155-191	2.29
*61	61	2.6	2.0	0.8	153	2.28
61	61	2.4	2.0-2.5	0.8	133-197	2.26
61	61	2.2	2.5-3.0	0.8	152-165	2.25
*61	62	2.5	2.0-4.0	0.6	167-171	2.27
61	60	3.1	2.0	0.9	180	2.32
61	60	2.9	2.0-2.5	0.9	165-187	2.30
*61	60	2.8	2.5	0.9	146	2.29

*Plotted in graph.

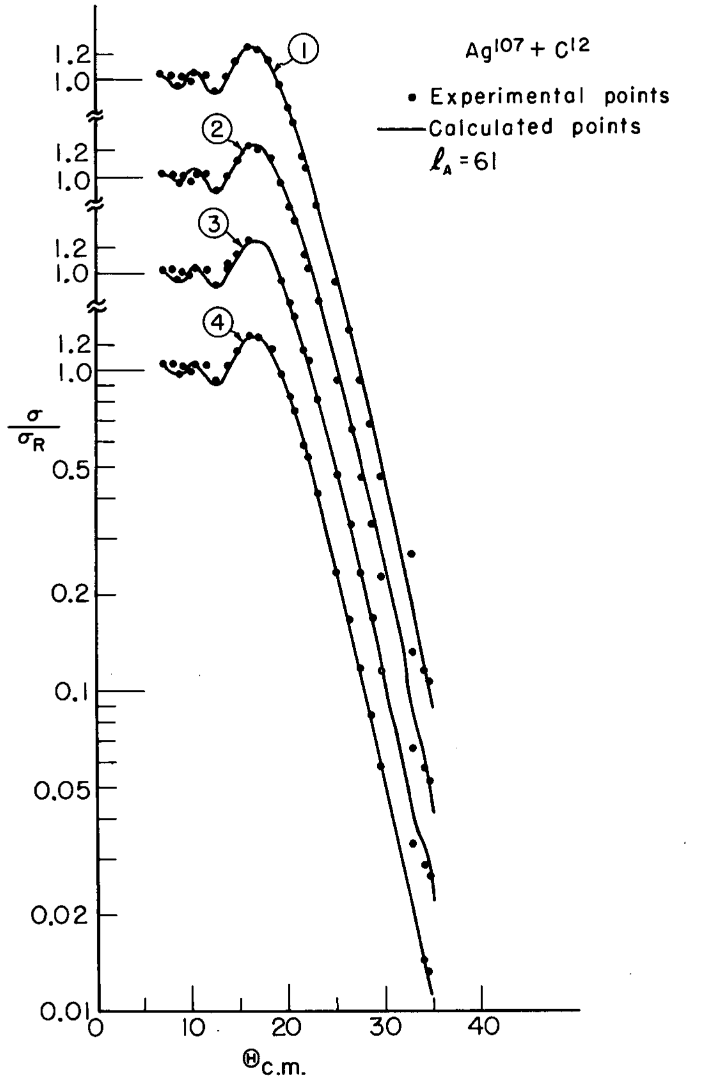

MU-23620

Fig. 19. Angular distribution of C^{12} ions elastically scattered from Ag^{107} at E_{lab} = 124.5 Mev. The dots are the measured cross sections and the solid line is the calculated cross section with the following McIntyre model parameters.

	ℓ_A	$\Delta\ell_A$	δ	ℓ_δ	$\Delta\ell_\delta$	Δ
(1)	61	2.5	0.7	61	2.5	167
(2)	61	2.5	0.6	62	2.0	167
(3)	61	2.6	0.8	61	2.0	153
(4)	61	2.8	0.9	60	2.5	146

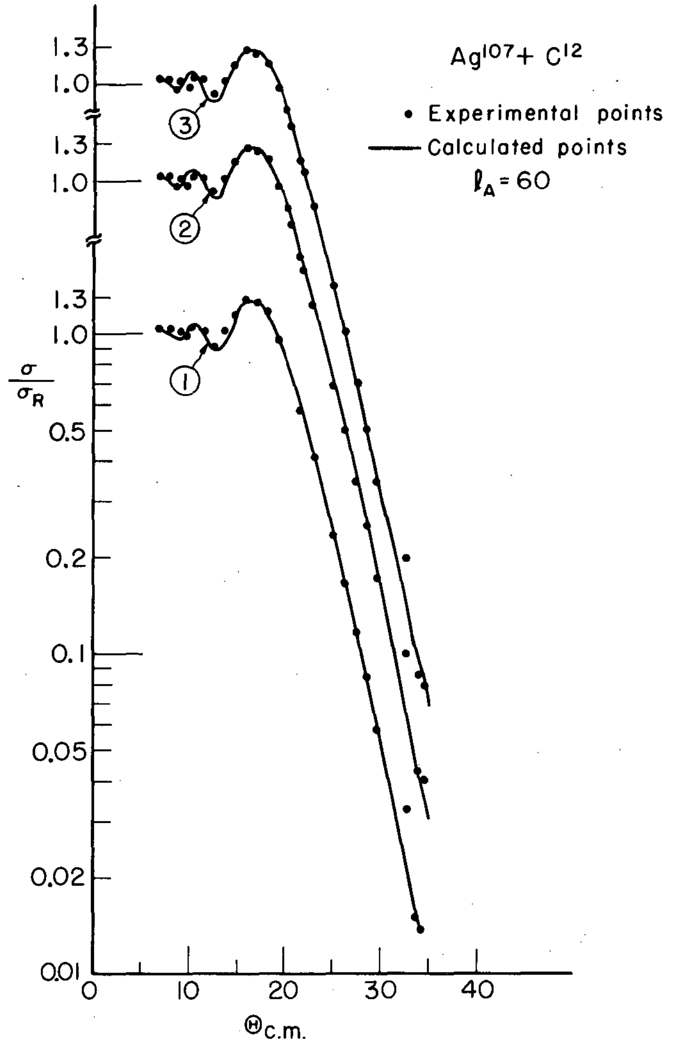

MU-23526

Fig. 20. Angular distribution of C^{12} ions elastically scattered from Ag^{107} at E_{lab} = 124.5 Mev. The dots are the measured cross sections and the solid line is the calculated cross section with the following McIntyre model parameters.

	ℓ_A	$\Delta\ell_A$	δ	ℓ_δ	$\Delta\ell_\delta$	Δ
(1)	60	2.5	0.8	60	2.5	190
(2)	60	2.2	0.7	61	3.0	162
(3)	60	2.4	0.9	60	2.5	151

D. Ni + C^{12}

The results for Ni + C^{12} are summed up in Tables VII and VIII, and in Fig. 21.

For $\ell_A = 54$: the interaction radius R $= (9.10 \pm 0.06) \times 10^{-13}$ cm.

For $\ell_A = 55$: the interaction radius R $= (9.25 \pm 0.06) \times 10^{-13}$ cm.

For $\ell_A = 56$: the interaction radius R $= (9.39 \pm 0.06) \times 10^{-13}$ cm.

For $\ell_A = 57$: the interaction radius R $= (9.59 \pm 0.06) \times 10^{-13}$ cm.

For $\ell_A = 54$: the surface parameter S is 1.94×10^{-13} cm.

For $\ell_A = 55$: the surface parameter S is $1.72 < S < 2.11 \times 10^{-13}$ cm.

For $\ell_A = 56$: the surface parameter S is $1.26 < S < 1.98 \times 10^{-13}$ cm.

For $\ell_A = 57$: the surface parameter S is $2.02 < S < 2.16 \times 10^{-13}$ cm.

Because of multiple scattering in the target is was not possible to measure the scattering at angles smaller than 5 deg in the laboratory system. For low-Z targets this means that the oscillation around $\sigma/\sigma_R = 1$ could not be measured, which introduces an error or several per cent in the normalization of σ/σ_R to unity. In this case, therefore, no attempt was made to vary all five parameters independently, and four ℓ_A values give equally good fits to the experimental data.

Table VII

Experimental results: Ni + C^{12}

$\theta_{c.m.}$ (deg)	$\left(\frac{d\sigma}{d\Omega}\right) / \left(\frac{d\sigma}{d\Omega}\right)_R$	Error	$\theta_{c.m.}$ (deg)	$\left(\frac{d\sigma}{d\Omega}\right) / \left(\frac{d\sigma}{d\Omega}\right)_R$	Error (%)
5.3	1.049	1	14.8	0.447	1
6.5	0.979	1	17.2	0.233	1
7.7	0.970	1	19.6	0.112	1.5
8.9	1.123	1	22.0	0.0533	1.5
9.1	1.133	1	23.4	0.0356	1.5
10.1	1.136	1	24.6	0.0253	1.5
10.3	1.190	1	25.8	0.0179	1.5
12.2	1.027	1	27.0	0.0137	2
12.4	0.810	1	28.2	0.0084	2
13.4	0.608				

Target thickness = 1.1 ± 0.05 mg/cm^2;

$\lambdabar$ = 0.144 f; $E_{c.m.}$ = 101.6 Mev; n = 8.28

Table VIII

Theoretical analysis: Ni + C^{12}

ℓ_A	ℓ_δ	$\Delta\ell_A$	$\Delta\ell_\delta$	δ	Δ	$\sigma_{Reaction}$ (b)
54	54	3.0	3.0	0.6	183	2.16
55	55	2.8	2.8	0.6	116	2.22
*55	55	3.0	3.0	0.5	147	2.23
55	55	3.0	3.0	0.6	178	2.23
55	55	3.2	3.2	0.5	160	2.25
55	55	3.4	3.4	0.4	189	2.27
56	56	2.8	2.8	0.5	154	2.29
56	56	2.8	2.8	0.6	146	2.29
*56	56	3.0	3.0	0.5	115	2.31
56	56	3.2	3.2	0.4	128	2.33
*57	57	3.2	3.2	0.4	137	2.40
57	57	3.4	3.4	0.3	145	2.42

*Plotted in graph.

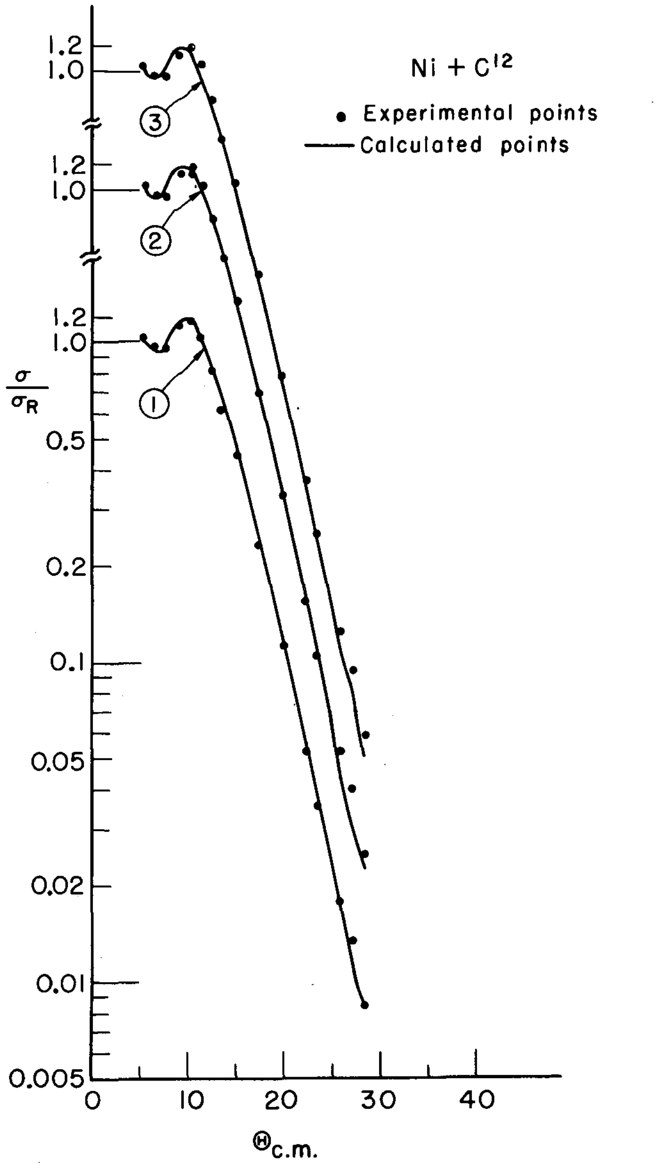

MU-23624

Fig. 21. Angular distribution of C^{12} ions elastically scattered from Ni at E_{lab} = 124.5 Mev. The dots are the measured cross sections and the solid line is the calculated cross section with the following McIntyre model parameters.

	ℓ_A	$\Delta\ell_A$	δ	ℓ_δ	$\Delta\ell_\delta$	Δ
(1)	55	3.0	0.5	55	3.0	147
(2)	56	3.0	0.5	56	3.0	115
(3)	57	3.2	0.4	57	3.2	137

E. Fe + C^{12}

The results for Fe + C^{12} are summed up in Tables IX and X, and Fig. 22.

For $\ell_A = 50$: the interaction radius R $= (8.51 \pm 0.05) \times 10^{-13}$ cm.

For $\ell_A = 51$: the interaction radius R $= (8.65 \pm 0.05) \times 10^{-13}$ cm.

For $\ell_A = 52$: the interaction radius R $= (8.80 \pm 0.05) \times 10^{013}$ cm.

For $\ell_A = 50$: the surface parameter S is $1.85 < S < 1.98 \times 10^{-13}$ cm.

For $\ell_A = 51$: the surface parameter S is $1.63 < S < 2.16 \times 10^{-13}$ cm.

For $\ell_A = 52$: the surface parameter S is $1.76 < S < 2.02 \times 10^{-13}$ cm.

The remarks made for Ni apply equally to this case.

Table IX. Experimental results: Fe + C^{12}

$\theta_{c.m.}$ (deg)	$\left(\frac{d\sigma}{d\Omega}\right) / \left(\frac{d\sigma}{d\Omega}\right)_R$	Error (%)	$\theta_{c.m.}$ (deg)	$\left(\frac{d\sigma}{d\Omega}\right) / \left(\frac{d\sigma}{d\Omega}\right)_R$	Error (%)
6.4	0.982	3.5	18.5	0.139	1
7.6	0.933	1	19.7	0.101	1
8.9	1.140	1	20.9	0.0734	1
10.1	1.104	1	22.1	0.0507	1
11.3	0.961	1	23.7	0.0238	1.5
12.5	0.723	1	25.0	0.0183	1.5
13.7	0.561	1	26.2	0.0131	2.5
14.9	0.373	1	27.4	0.00885	3
16.1	0.302	1	28.6	0.00575	3.5
17.3	0.200	1			

Target thickness = 1.9 ± 0.3 mg/cm^2;

$\lambda\!\!\!^{-}$ = 0.145 f; $E_{c.m.}$ = 100.8 Mev; n = 7.69.

Table X

Theoretical analysis: Fe + C^{12}

ℓ_A	ℓ_δ	$\Delta\ell_A$	$\Delta\ell_\delta$	δ	Δ	σ_{Reaction} (b)
*50	50	2.8	2.8	0.75	247	1.89
50	50	3.0	3.0	0.6	323	1.90
50	50	3.2	3.2	0.6	299	1.92
51	51	2.6	2.6	0.75	214	1.94
51	51	2.8	2.8	0.6	285	1.96
*51	51	3.0	3.0	0.6	195	1.97
51	51	3.4	3.4	0.45	274	2.00
*52	52	2.8	2.8	0.6	151	2.03
		3.0	3.0	0.6	171	2.05
		3.2	3.2	0.45	191	2.06

---

*Plotted in graph.

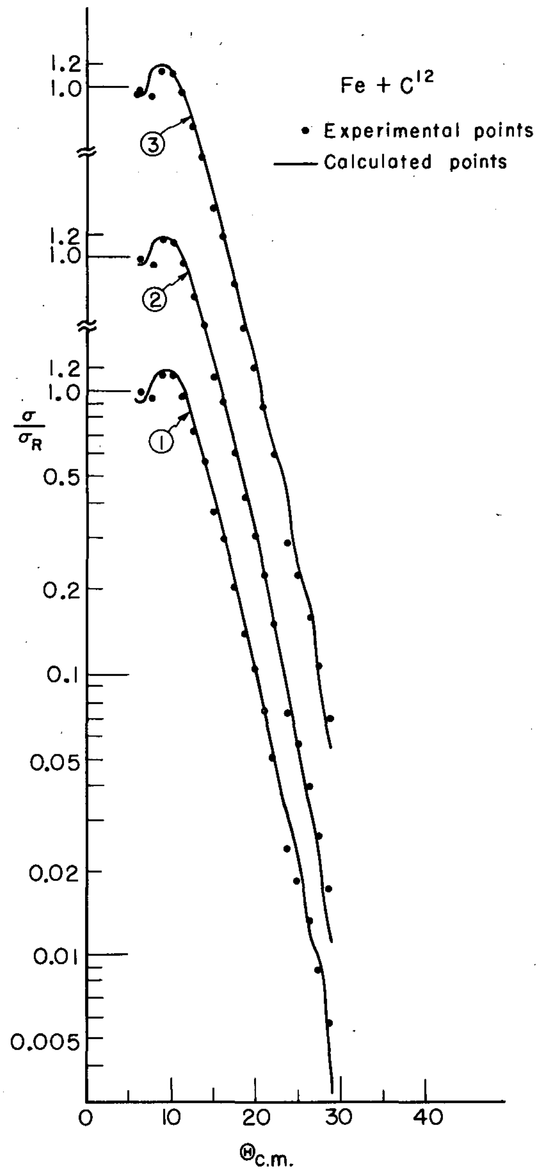

MU-23623

Fig. 22. Angular distribution of C^{12} ions elastically scattered from Fe at E_{lab} = 124.5 Mev. The dots are the measured cross sections and the solid line is the calculated cross section with the following McIntyre model parameters.

	ℓ_A	$\Delta\ell_A$	δ	ℓ_δ	$\Delta\ell_\delta$	Δ
(1)	50	2.8	0.75	50	2.8	247
(2)	51	3.0	0.6	51	3.0	195
(3)	52	2.8	0.6	52	2.8	151

F. A + C^{12}

The cross sections in Table XI are relative cross sections. In this case only a small part of the initial rise could be measured, therefore no fits with the McIntyre model are given since many combinations of parameters can be found that will reproduce just the slope of the fall-off from Rutherford scattering.

Table XI

Experimental results: A + C^{12}

θ c.m. (deg)	$\left(\frac{d\sigma}{d\Omega}\right)\left(\frac{d\sigma}{d\Omega}\right)_R$	Error (%)
5.6	.23	3
6.9	7.13	1
8.2	5.98	1.5
9.5	4.46	1.5
10.8	3.17	1.5
12.1	2.00	1.5
13.4	1.45	1.5
14.7	1.01	2
16.0	0.719	2.5
17.3	0.482	2
18.6	0.350	3
21.1	0.184	4.5
22.4	0.125	4.5

Target thickness varies with angle;

$\lambdabar = 0.173 \times 10^{-13}$ cm; $E_{c.m.}$ 75.4 Mev; n = 5.91

IV. DISCUSSION OF RESULTS

Heavy-ion elastic scattering experiments were first done with 27-Mev N^{14} ions by Reynolds and Zucker.[34] Halbert and Zucker later carried out similar experiments.[35, 36, 37] Goldberg and Reynolds[38] bombarded Au^{197} with C^{12} ions of different energies, and Kerlee and others scattered C^{12}, N^{14}, O^{16}, and Ne^{20} from Au^{197} and Bi^{209} (see Ref. 39), using photographic detection of the scattered particles. The authors obtained reasonable fits with the Blair model. Similar experiments with O^{16} ions on several targets have been made by McIntyre et al.,[40] using detection in CsI scintillation counters. All these results follow the same trend as the angular distributions found in the present work. In our experiments emphasis has been given to measuring the angular distributions with 1% statistics, in order to bring out the details in the structure. Blair's semiclassical sharp-cutoff model for elastic scattering can reproduce the small-angle part of the experimental angular distributions, but for larger angles the Blair model gives strong oscillations because of the sharp-cutoff at the classical distance of closest approach of the two nuclei. In elastic α-scattering experiments it has been found[3] that these large oscillations start at angles where $\sigma/\sigma_R \approx 1/n$. As has been pointed out in Sec. I, the sharp-cutoff model is expected to be better for heavy ions than for α particles, because for heavy ions the scattering is "more classical". These experiments show, however, that $(\sigma/\sigma_R)_{\text{calculated}}$ starts deviating already for angles where $(\sigma/\sigma_R)_{\text{measured}} > 1/n$ (see Fig. 3). In the region of small angles, the sharp-cutoff model cannot account for the details in the structure around $\sigma/\sigma_R = 1$; in particular the initial rise in the Blair model decreases continuously with decreasing Z of the target, whereas in our experiments the rise does not vary with Z in any regular way.

In the McIntyre model, the sharp-cutoff is replaced by a smooth decrease over many ℓ waves; and a smoothly varying real phase shift δ_ℓ is introduced, in addition to the Coulomb phase shift (see Sec. I). Figures 15-22 show that very good agreement can be obtained between this model and the experiments.

All important features of the experimental angular distributions can be reproduced by using only three of the five available parameters, making $\ell_A = \ell_\delta$ and $\ell_A = \Delta\ell_\delta$. The large initial rise for Ag^{107} and In can be fitted by making δ_ℓ large. In most cases $\Delta\ell_A \geqslant 2$; for $\Delta\ell_A < 2$ strong oscillations appear again, although at larger angles than in the sharp-cutoff model. By varying all five parameters independently, refinements in the fits can be made such that in some cases all calculated cross sections fall inside the statistical errors of the measured cross sections.

The results derived from the analysis are tabulated in Table XII. Column 1 gives the interaction radius obtained by averaging the radii derived from all the possible ℓ_A values. The error indicated is the maximum error.

Column 3 gives the surface parameter obtained in the analogous way as Column 1.

R_0 in Column 2 is the same in all cases except for Ni. The R_0 value agrees very well with the value 1.46×10^{-13}cm derived with the sharp-cutoff by Kerlee, Goldberg, and Reynolds[39] for the scattering of C^{12}, N^{14}, O^{16}, and Ne^{20} from Au^{197} and Bi^{209}.

The large deviation of R_0 for Ni may be explained by the fact that no distinction in goodness of fit for four ℓ_A values could be made, which causes the error in this case to be rather large.

The surface parameter S is roughly the same in all cases. McIntyre compared the elastic scattering of F^{19} from Tb with O^{16} from Pb^{208} having a diffuse and a sharp boundary respectively.[16, 19] He found that the surface parameter for the Tb+F system is about twice that for the Pb+O system. From all these results one can conclude that the McIntyre analysis of elastic scattering data is a good probe for measuring the surface region of nuclei, giving large surface parameters for "diffuse systems" (Tb + F) and smaller, constant surface parameters for other systems. The total reaction cross sections compiled in Column 4 are obtained by averaging the values in the tables. The errors include all the possible values of the tables.

The reaction cross sections agree very well with the formula

$$\sigma_R \approx \pi (R + \lambda)^2 \left[1 - V(R + \lambda)/E \right]$$

given by Blatt and Weisskopf,[41] where

$$V(R + \lambda) = Z_1 Z_2 e^2/(R + \lambda),$$

which is not surprising, since in the derivation of this formula essentially the same assumptions are made as in the Blair model.

Table XII

Results derived from McIntyre analysis

	R	$R_0 = \frac{R}{A_1^{1/3} + A_2^{1/3}}$	S	σ_{Reaction} (b)
Ta	11.57 ± 0.14	1.45 ± 0.02	1.63 ± 0.40	2.43 ± 0.03
In	10.30 ± 0.12	1.44 ± 0.02	1.19 ± 0.18	2.20 ± 0.05
Ag^{107}	10.15 ± 0.12	1.44 ± 0.02	1.36 ± 0.22	2.23 ± 0.07
Ni	9.32 ± 0.30	1.51 ± 0.05	1.94 ± 0.22	2.29 ± 0.15
Fe	8.65 ± 0.20	1.42 ± 0.03	1.89 ± 0.26	2.14 ± 0.10

V. THE RAINBOW MODEL

Our elastic scattering data for Ni, Ag^{107}, In, and Ta have recently been analyzed with the Ford Wheeler rainbow model,[42] by M. V. Goldman at the Oak Ridge National Laboratory.[43] Only a very brief description of this semiclassical model is given here because very good exposes are available in the literature,[42, 44]

The classical, qualitative behavior of the scattering angle as a function of angular momentum ℓ, the "deflection function," is shown in Fig. 23. When the classical impact parameter is large, corresponding to large ℓ, the deflection function is small (see also Fig. 1); it follows the classical repulsive Coulomb deflection function until the impact parameter becomes small enough for the projectile to be attracted by the nuclear forces. Consequently, a maximum θ_R in the deflection function will occur at ℓ_R. (In geometrical optics, an extremum in the deflection function gives rise to a rainbow.[45]) For impact parameters such that $\ell < \ell_s$ the particle is fully absorbed, which corresponds classically to spiraling inside the nucleus.

Starting from the quantum-mechanical equation for the scattering amplitude,

$$f(\theta) = \frac{\lambda}{2i} \sum_{\ell=0}^{\infty} (2\ell+1)(e^{2i\sigma_\ell} - 1) P_\ell(\cos\theta),$$

one can calculate the cross section for elastic scattering by making the following approximations

(a) the phase shifts σ_ℓ are evaluated by the WKB method;

(b) the asymptotic form for the Legendre polynomials is used; and

(c) the summation is replaced by an integration.

If, furthermore, the deflection function in the neighborhood of θ_R is approximated by

$$\theta(\ell) = \theta_R - q(\ell - \ell_R)^2,$$

the cross section divided by the Rutherford cross section becomes

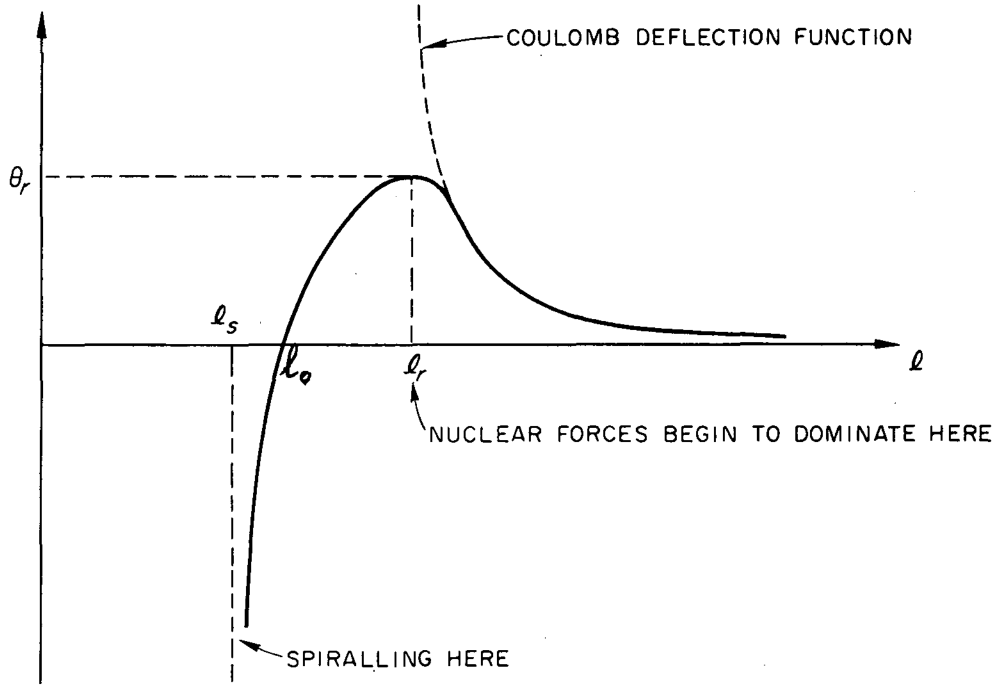

MU-23535

Fig. 23. Classical deflection function vs angular momentum without absorption (from Ref. 43).

$$\frac{\sigma}{\sigma_R} = \frac{2 \sin^2 \frac{1}{2} \theta_R}{n\, q^{2/3}} \; 2\pi \, \mathrm{Ai}(x) \; ,$$

where $x = q^{-1/3} (\theta_R - \theta)$, and $\mathrm{Ai}(x)$ is the Airy integral. Here, q and θ_R are used as free parameters, in order to fit measured angular distributions.

A nuclear radius can be defined as the distance of closest approach for Coulomb scattering at the angle θ_R. So with Eq. (1.2) one gets

$$R = \left(Z_1 Z_2 e^2/2E\right) / \left(1 + \operatorname{cosec} \frac{1}{2} \theta_R\right)$$

The distance corresponding to $\Delta \ell = \ell_R - \ell_S$ can be regarded as a refractive nonaborptive surface region. Since ℓ_S is not known, one takes $\Delta_\ell = \ell_R - \ell_0$, and the surface region is $\Delta R = \frac{\Delta \ell}{k}$, where k is the wave number.

Goldman's rainbow-model fits to our data are shown in Fig. 24, together with the parameters and the derived values for $r_0 = R/A^{1/3}$, and ΔR. One sees that the fits are good for angles $\theta > \theta_R$ but fail at smaller angles. The r_0 values are only slightly larger than the values in Table XII, but ΔR is larger than the surface parameters S found in Sec. III. This is of course not surprising, because the surface regions in the two models are defined in different ways. In the rainbow model no absorption is assumed for ℓ larger than ℓ_S.

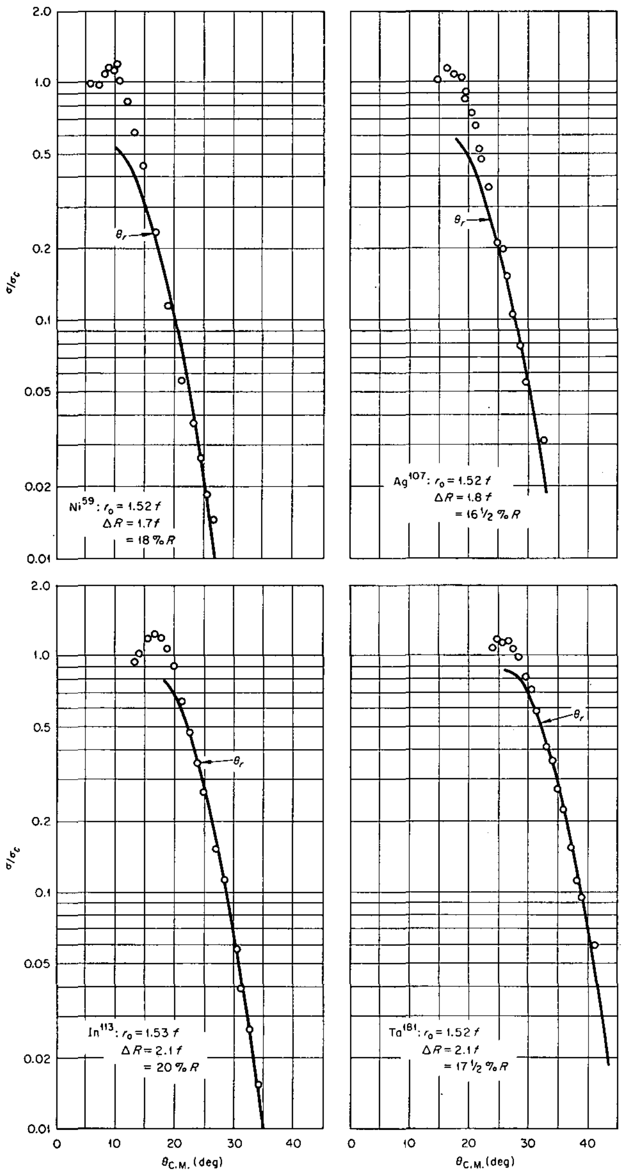

MU-23536

Fig. 24. Rainbow model fits for C^{12} elastically scattered from Ni, Ag^{107}, In, and Ta (from Ref. 43).

VI. COMPARISON OF THE MCINTYRE AND OPTICAL MODELS

The optical model describes the nucleus by a complex potential where the imaginary part allows for absorption of incident particles by the nucleus. The wave function of the nucleus-particle system is calculated by solving (numerically) the Schrödinger equation and, combined with boundary conditions, complex phase shifts are calculated. The elastic scattering cross section can then be found with a formula analogous to Eq. (1.11).

The optical model was introduced to describe neutron reaction cross sections and was later adapted to proton scattering,[46, 47, 48] α-particle scattering,[49, 50] and recently to heavy-ion scattering.[51, 52] The potential used for charged-particle scattering has the general form

$$\left(V_0 + i\,W_0\right) / \left\{1 + \exp\left[(r - R)/d\right]\right\} + V_{coul} + V_{centr} ,$$

where V_0 is the depth of the real part of the optical potential; W_0 is the depth of the imaginary part of the optical potential; r is the distance to the center of the nucleus; R is the radius of the nucleus (this definition need not necessarily give the same quantity as the definition in earlier sections); d defines the surface thickness; V_{coul} is the Coulomb potential; and V_{centr} is the centrifugal potential.

A potential of this form has been very successful in describing the scattering of protons and α particles, and moderately successful for the few heavy-ion experiments that have been analyzed.

The independent parameters used in the optical model to fit the experimental data are V_0, W_0, R, and d, respectively a measure for the strength of the nuclear potential, the strength of the absorption, the nuclear radius, and the diffuseness of the surface.

It has been shown in Sec. IV that the McIntyre model is capable of giving the analogous information on the nucleus-projectile system, by inserting parameters directly in the phase shifts instead of in the potential. It seems therefore of interest to compare the two models in some detail. For this purpose we analyzed with the McIntyre model the existing elastic-scattering data of 18-Mev alpha particles from A,[53] 40-Mev alpha particles from Cu,[54] and 48-Mev alpha particles from Pb,[14] which have previously been analyzed with an optical model by Igo,[55] and the elastic scattering of 27-Mev N^{14} ions from Be and

C^{12} by Halbert and Zucker,[35, 36] which have been analyzed with the optical model by Drisko and Bassel.[52] Figures 25 through 29 show the fits to experimental data with the McIntyre model, together with the optical-model fits. In all cases the fits are comparable; in some cases one model gives a better agreement than the other, depending to some extent on what feature of the curve is regarded as most significant.

The parameters for the two models are compiled in Table XIII, together with the analyses of 40-Mev alpha particles on Ag from Cheston and Glassgold[49] and McIntyre et al.[15] It is not surprising that the values for the radii and the surface regions are not the same in both models, since they are differently defined. Since the cross section in both models is calculated from the phase shifts, we plotted in Fig. 30 the real part of the nuclear phase shift and the absorption factors[56] $T_\ell = 1 - |\exp[2i\,\delta_\ell]|^2$ as a function of ℓ for the elastic scattering of alpha particles from Pb according to the McIntyre and optical models.[57]

The absorption coefficients are nearly identical for the two models. For ℓ values larger than about 20 the real phase shifts are also identical, but for smaller ℓ's they are dramatically different. Since the absorption curve shows that the partial waves for $\ell < 13$ are completely absorbed, one may say that the real phase shift for these partial waves is irrelevant to the elastic scattering cross section.

In order to test this contention, angular distributions were calculated with the McIntyre model for alpha particles scattered from Cu, arbitrarily setting the real part of δ_ℓ equal to zero for ℓ values ranging from 1 to 20. Figure 31 shows the results of these calculations. The cross sections are not affected at all by cutting off $\mathrm{Re}\,\delta_\ell$ for ℓ up to 13; cutting it off for 14 ℓ's brings a small change in the cross section, but not until ℓ values are cut off, for which $T_\ell < 1$, is the angular distribution seriously distorted.

These results provide a support for the semiclassical arguments that small ℓ waves are completely absorbed and that the main contribution to the shape of the angular distribution comes from the surface region, where the curves in Fig. 30 coincide.

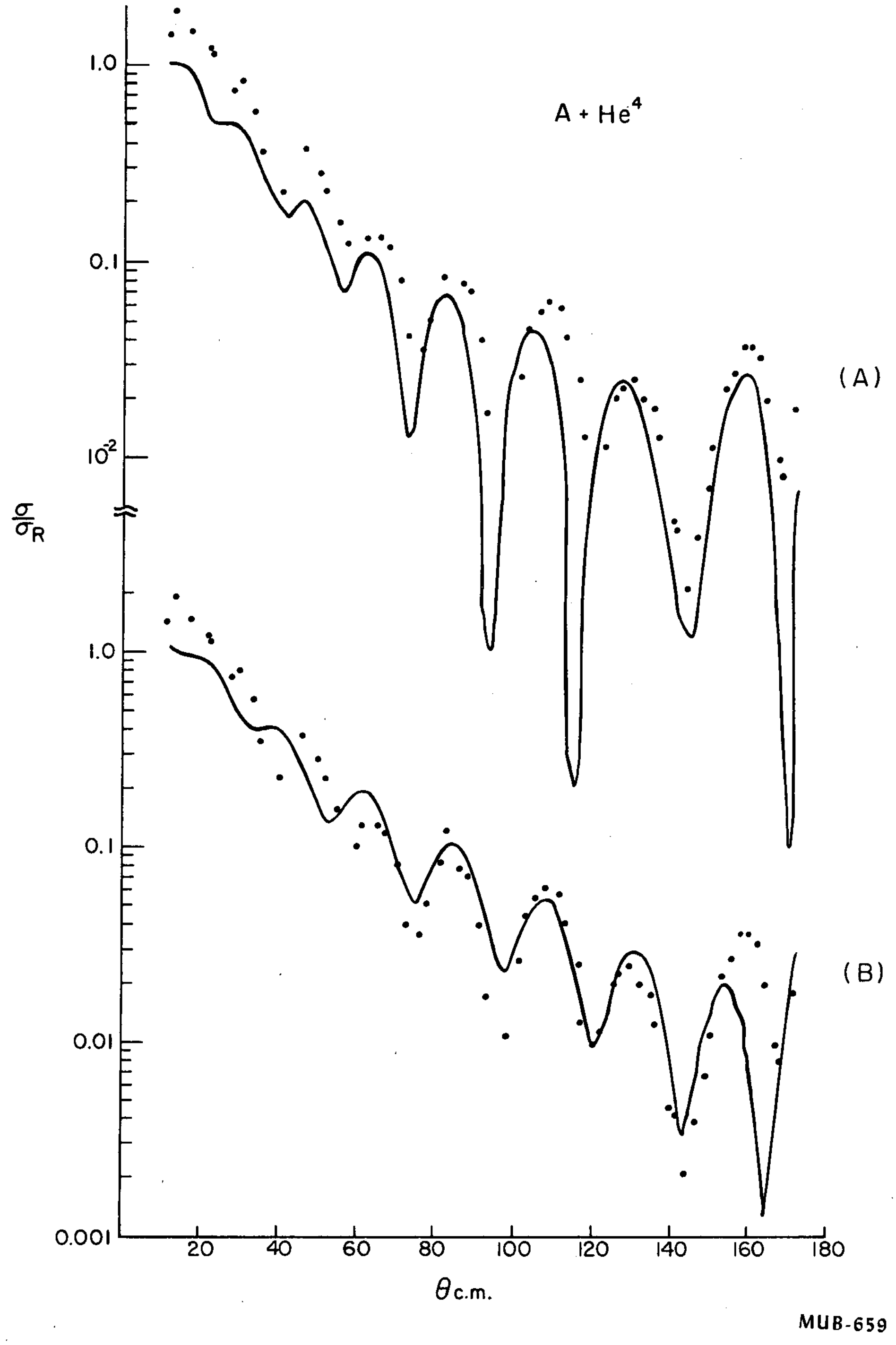

Fig. 25. (A) The solid line is the optical-model fit to the elastic scattering of α's from A (Ref. 55). Parameters are $V_0 = 100$, $W_0 = -15$, $R = 1.17A^{1/3} + 1.36$, $d = 0.6$. The points give the experimental values.

(B) The solid line gives the McIntyre model fit to the same data with the parameters $\ell_A = 7.5$, $\Delta\ell_A = 0.6$, $\delta = 1.2$, $\ell_\delta = 6.5$, $\Delta\ell_\delta = 0.5$.

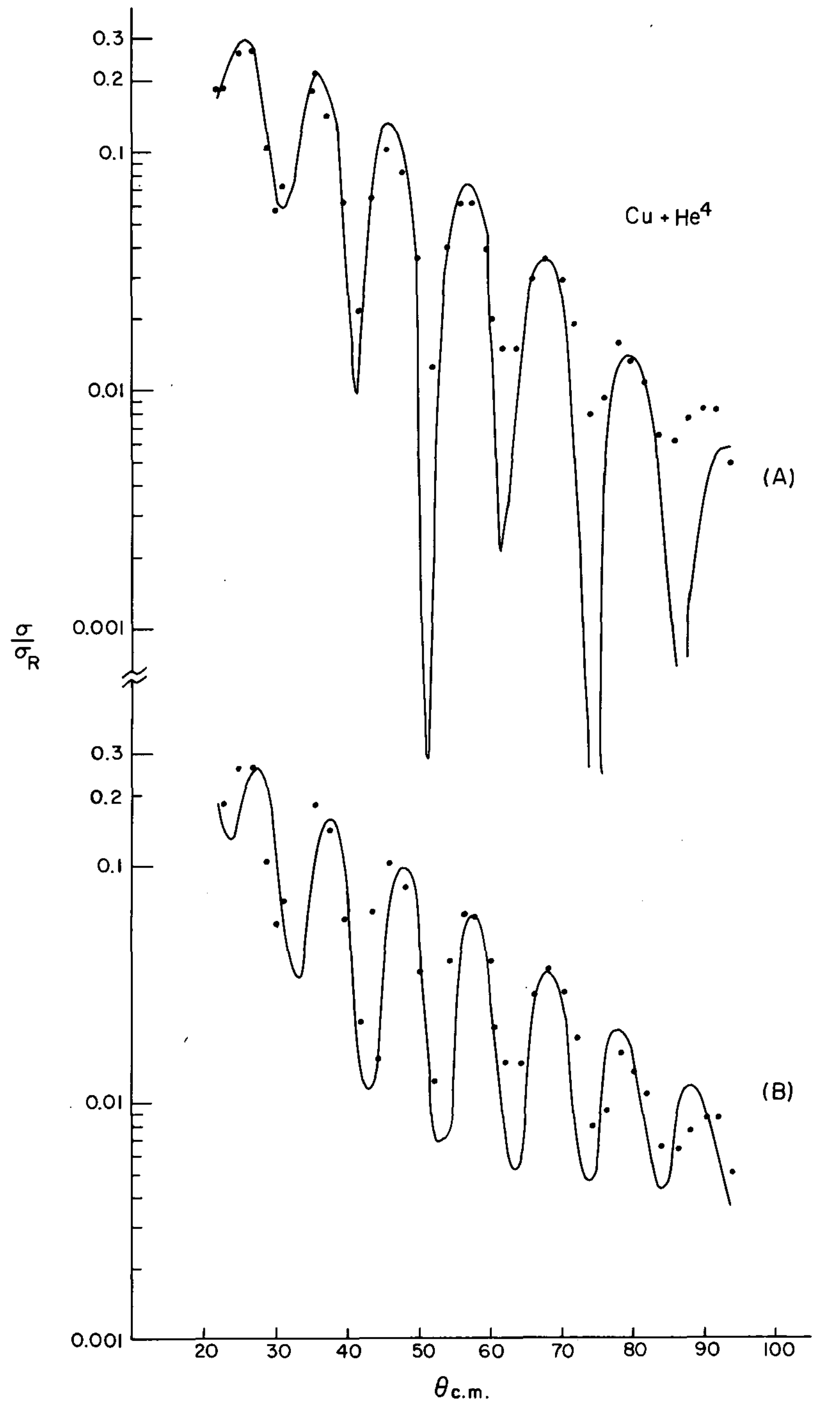

Fig. 26. (A) Same as 25(A) for α's scattered from Cu (Ref. 55), The parameters are V_0 = - 49.3, W_0 = - 11, R = $1.14A^{1/3}$ + 2.24, d = 0.5.

(B) Same as 25B (Ref. 55). The parameters are ℓ_A = 17, $\Delta\ell_A$ = 0.8 , δ = 0.7, ℓ_δ = 17, $\Delta\ell_\delta$ = 1.0.

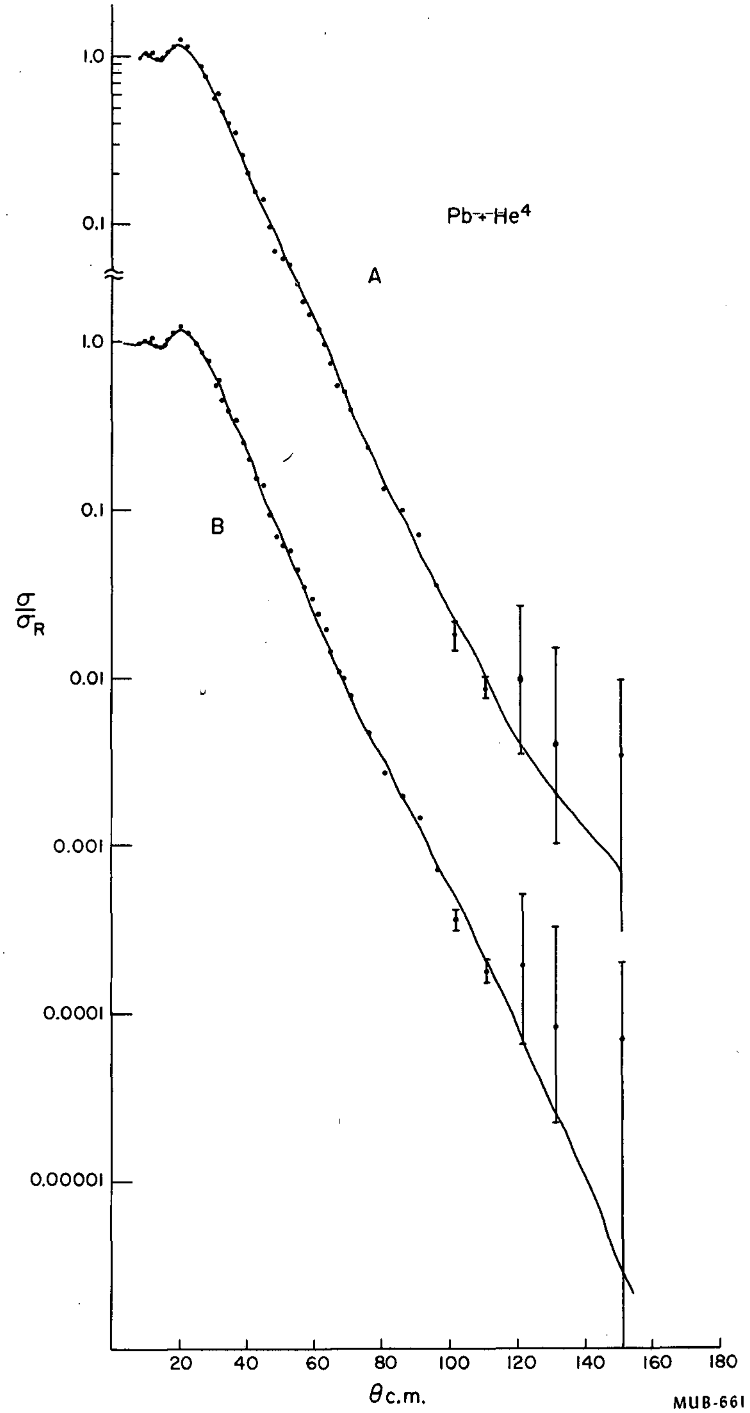

Fig. 27. (A) Same as 25A for α's scattered from Pb (Ref. 55). The parameters are $V_0 = -25$, $W_0 = -15$, $R = 1.13A^{1/3} + 2.0$ $d = 0.6$.

(B) Same as 25B. The parameters are $\ell_A = 21$, $\Delta\ell_A = 1.3$, $\delta = 0.2$, $\ell_\delta = 23$, $\Delta\ell_\delta = 1.4$.

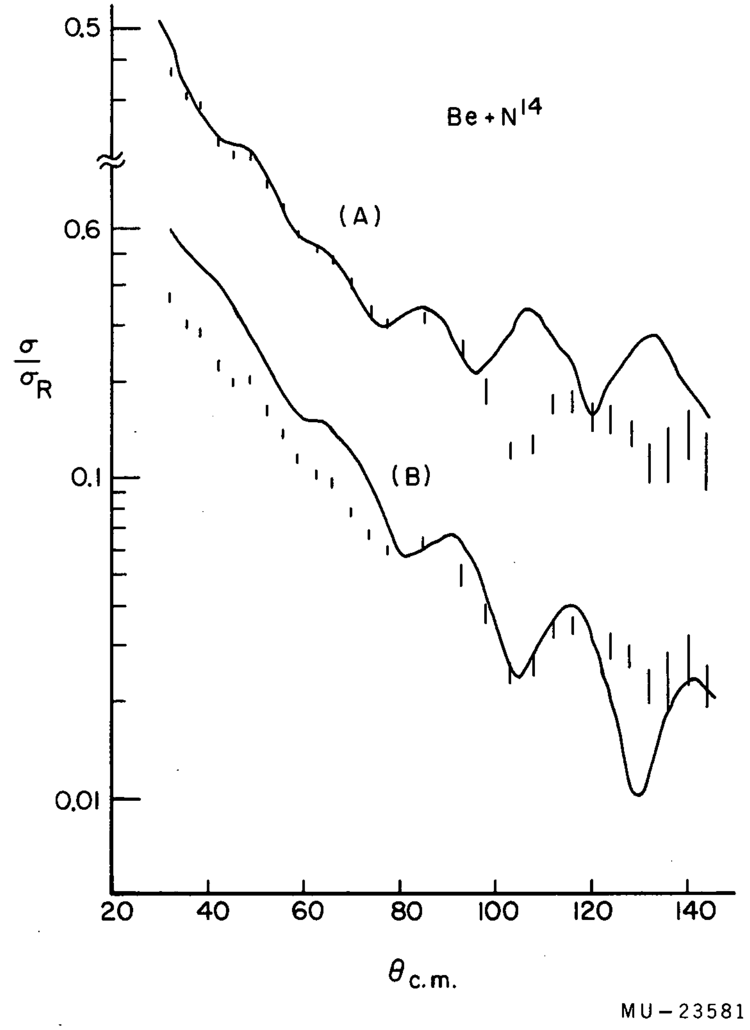

Fig. 28. (A) Same as 25A for N^{14} scattered from Be (Ref. 52). The parameters are $V_0 = -50$, $W_0 = -16$, $R = 1.23A^{1/3}$, $b = 1.125$, $d = 0.65$.

(B) Same as 25 B. The parameters are $\ell_A = 7.5$, $\Delta\ell_A = 0.8$, $\delta = 0.8$, $\ell_\delta = 6.5$, $\Delta\ell_\delta = 0.3$.

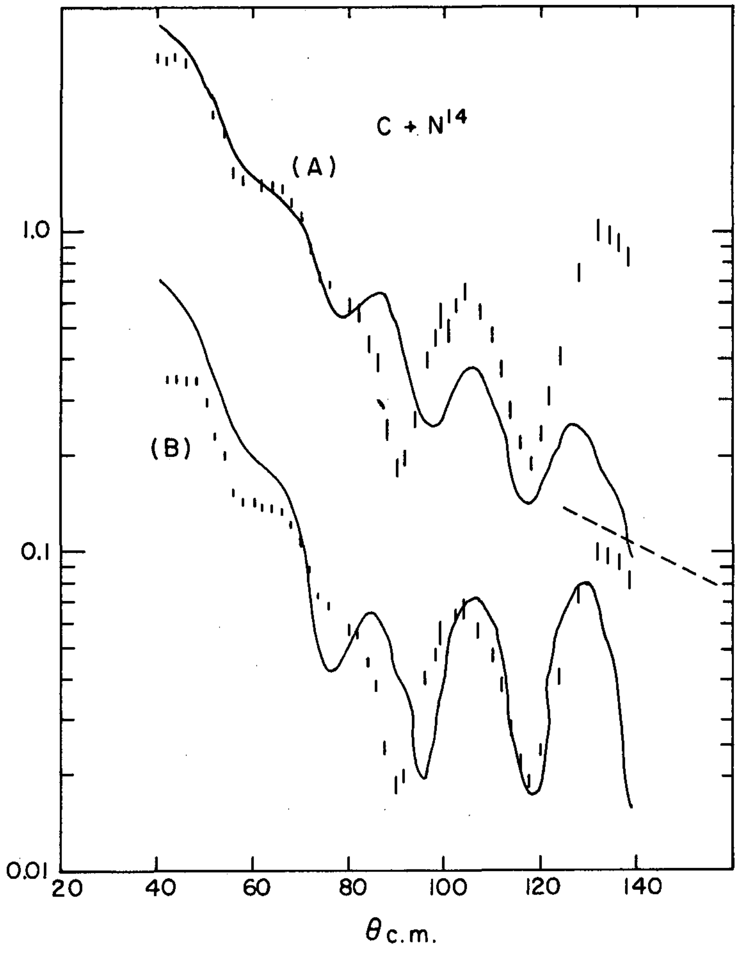

MU-23582

Fig. 29. (A) Same as 25A for N^{14} scattered from C. The parameters are $V_0 = -48$, $W_0 = -5.75$, $R = 1.275A^{1/3}$, $d = 0.575$.

(B) Same as 25B. The parameters are $\ell_A = 8.2$, $\Delta\ell_A = 1.4$, $\delta = 0.9$, $\ell_\delta = 7.3$, $\Delta\ell_\delta = 0.2$.

Table XIII

Comparison of the McIntyre and optical models

	McIntyre Model								Optical Model						
	ℓ_A	$\Delta\ell_A$	δ	ℓ_δ	$\Delta\ell_\delta$	S 10^{-13} cm	R_0 10^{-13} cm	σ_R(b)	V_0	W_0	R 10^{-13} cm	4.4d 10^{-13} cm	R_0 10^{-13} cm	σ_R (b)	S_{opt} [a]
A + He^4	7.5	0.6	1.2	6.5	0.5	1.45	1.33	0.83	-100	-15	$1.17A^{1/3} + 1.36$	2.6	1.44	1.34	1.60
Cu + He^4	17	0.8	0.7	17	1.0	1.32	1.42	1.55	- 49.3	-11	$1.14A^{1/3} + 2.24$	2.2	1.54	1.72	1.37
Pb + He^4	21	1.3	0.2	23	1.4	1.80	1.35	1.85	- 25	-15	$1.13A^{1/3} + 2.0$	2.6	1.45	1.89	2.00
[a]Ag + He^4	19	1.1	0.3	19	1.6	1.76	1.46		- 50	-20	7.5	2.6	1.18		1.52
Be + N^{14}	7.5	0.8	0.8	6.5	0.3	1.89	1.60	0.89	- 50[b]	-16	$1.23A^{1/3}$;b = 1.125	(2.86)	1.23		
C + N^{14}	8.2	1.4	0.9	7.3	0.2	2.73	1.58	0.86	- 48	- 5.75	$1.275A^{1/3}$	2.53	1.275		

[a] From Refs. 15 and 49.

[b] In this case, the imaginary potential has a Gaussian shape, and b is the standard deviation (see Ref. 52).

[c] For explanation, see page 79 .

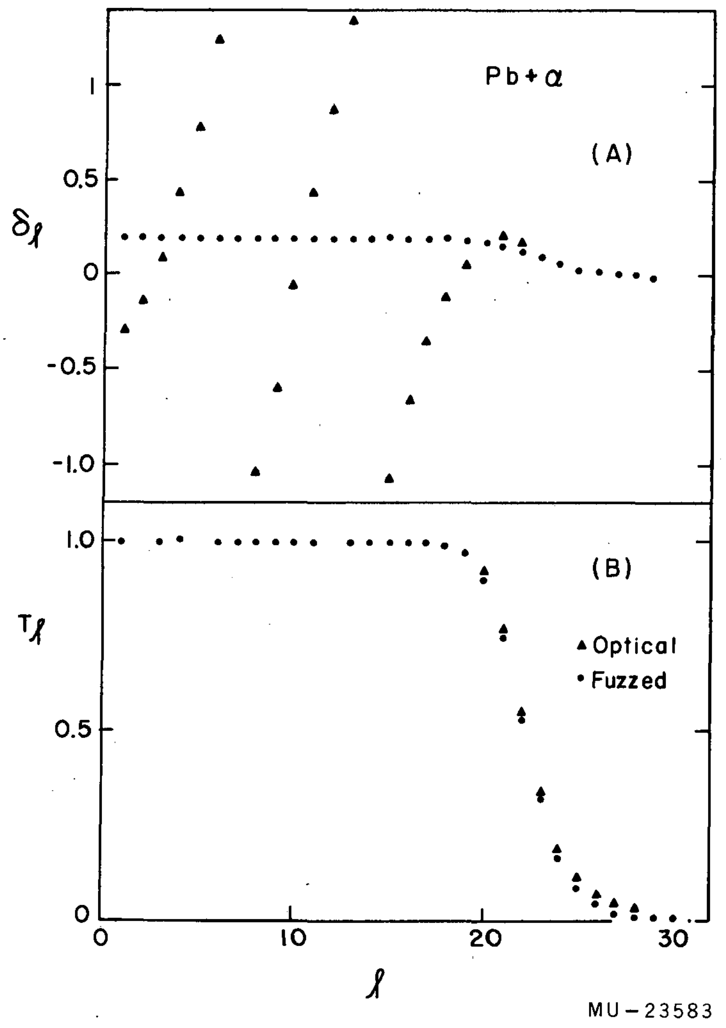

Fig. 30. (A) The real part of the phase shifts is plotted as a function of ℓ for the optical model (●) and the McIntyre model (▲), for α's scattered from Pb.

(B) The absorption factor $T_\ell = 1 - |e^{2i\delta_\ell}|^2$ is plotted as a function of ℓ for the optical model (●) and the McIntyre model (▲), for α's scattered from Pb.

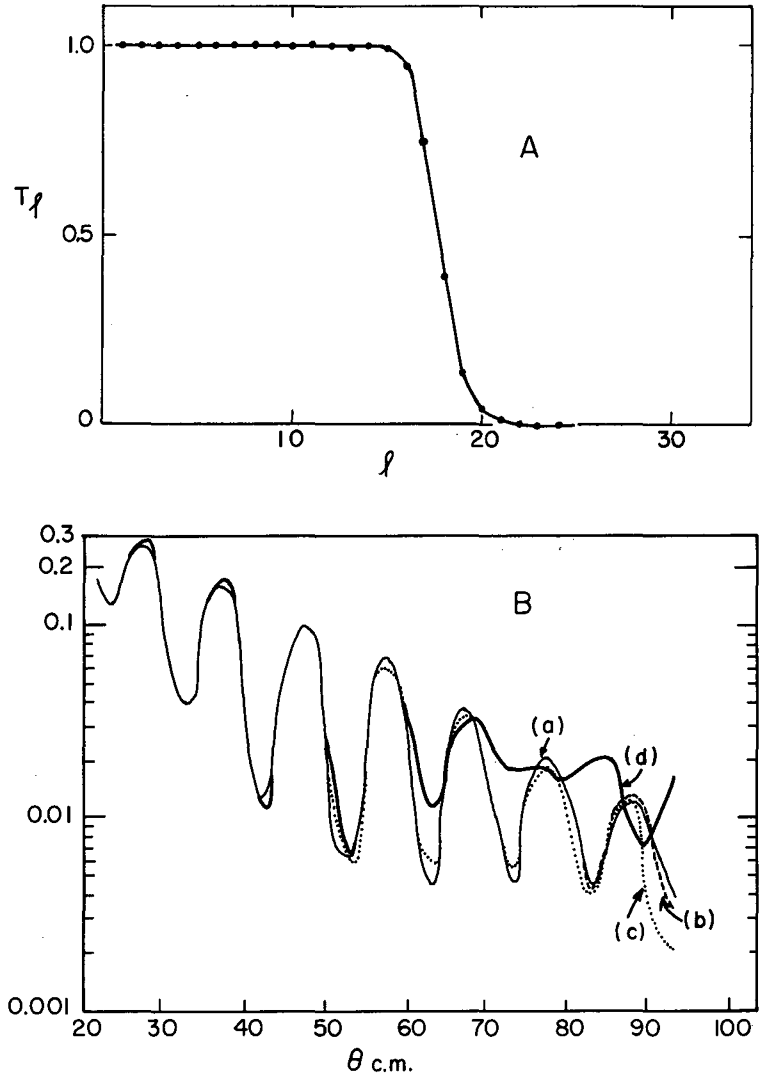

MU-23584

Fig. 31. (A) The absorption factor T_ℓ is plotted as a function of ℓ for the McIntyre model, for α's scattered from Cu.

(B) The solid line$^{\underline{a}}$ gives the cross section calculated with the McIntyre model with the parameters $\ell_A = 17$, $\Delta\ell_A = 0.8$, $\delta = 0.7$, $\ell_\delta = 17$, $\Delta\ell_\delta = 1.0$.
Line b gives the same calculation, making $\delta_\ell = 0$ for $\ell < 14$;
Line c gives the same calculation, making $\delta_\ell = 0$ for $\ell < 15$;
Line d gives the same calculation, making $\delta_\ell = 0$ for $\ell < 16$.

The same effect was found by Igo,[55] who noticed that in his optical-model analyses all the different potentials that give a good fit to the experimental data coincide at the surface of the nucleus. In the optical-model computation it is therefore not necessary to start the integration of the Schrödinger equation at the center of the nucleus. The present results, moreover, show that it is not necessary to integrate for ℓ waves below ℓ for which $T_\ell \neq 1$; this is a great advantage, especially in heavy-ion scattering analysis.

From the absorption factors, computed with the optical model, one can now calculate the surface region in a manner which is more consistent with the way the surface region was defined in Sec. I as follows: $S_{\mathrm{opt}} = \Delta\ell/k$, where $\Delta\ell$ is the range over which the value of

$\left| \exp \left\{ 2i\, \delta_\ell \right\} \right|$ changes from 0.9 to 0.1, and k is the wave number. The

values for the surface region calculated this way are shown in column 15 of Table 13.

APPENDICES

Appendix A. Derivation of Scattering Cross Section Formulas

The general formula for elastic scattering cross section is:

$$\sigma(\theta) = \left| f(\theta) \right|^2 . \tag{A.1}$$

In expansion of partial waves:

$$f(\theta) = \frac{\lambda\!\!\!^{-}}{2i} \sum_{\ell=0}^{\infty} (2\ell+1)(\eta_\ell - 1) P_\ell(\cos\theta). \tag{A.2}$$

For Coulomb scattering

$$\eta_\ell = e^{2i\sigma_\ell} ; \quad \sigma_\ell = \arg \Gamma\ (1 + \ell + in) \tag{A.3}$$

The Coulomb scattering amplitude can also be calculated exactly:

$$f_c(\theta) = \frac{\lambda\!\!\!^{-} n}{2 \sin^2 \frac{\theta}{2}} \, e^{-in\ln(\sin^2 \frac{\theta}{2}) + i\pi + 2i\sigma_0} . \tag{A.4}$$

1. Derivation of Equation (1.11)

In the McIntyre model,

$$\eta_\ell = A_\ell \, e^{2i(\sigma_\ell + \delta_\ell)} . \tag{A.5}$$

$$f(\theta) = \frac{\lambda\!\!\!^{-}}{2i} \sum_{\ell=0}^{\infty} (2\ell+1)(A_\ell \, e^{2i(\sigma_\ell+\delta_\ell)} - 1) P_\ell(\cos\theta);$$

$$f(\theta) = \frac{\bar{\lambda}}{2i} \sum_{\ell=0}^{\infty} (2\ell+1)\left(e^{2i\sigma_\ell}-1\right) P_\ell(\cos\theta)$$

$$+\frac{\bar{\lambda}}{2i} \sum_{\ell=0}^{\infty} (2\ell+1)\, e^{2i\sigma_\ell}\left(A_\ell\, e^{2i\delta_\ell}-1\right) P_\ell(\cos\theta).$$

(A.6)

Using (A.2), (A.3), and (A.4):

$$f(\theta) = \frac{\bar{\lambda}}{2}\left[-\frac{n}{\sin^2\frac{\theta}{2}}\, e^{-in\ln(\sin^2\frac{\theta}{2})+2i\sigma_0}\right]$$

$$+\frac{\bar{\lambda}}{2i} \sum_{\ell=0}^{\infty} (2\ell+1)\, e^{2i\sigma_\ell} P_\ell(\cos\theta)\left(A_\ell\, e^{2i\delta_\ell}-1\right);$$

$$\sigma(\theta) = |f(\theta)|^2 = \frac{\bar{\lambda}^2}{4}\left|\, e^{2i\sigma_0} \times\right.$$

$$\left.\left\{\frac{n}{\sin^2\frac{\theta}{2}}\, e^{-in\ln(\sin^2\frac{\theta}{2})} + i\sum_{\ell=0}^{\infty} (2\ell+1)\, e^{2i(\sigma_\ell-\sigma_0)}\left(A_\ell\, e^{2i\delta_\ell}-1\right)P_\ell(\cos\theta)\right\}\right|^2.$$

Total Coulomb cross section $\sigma_c(\theta) = \frac{\bar{\lambda}^2}{4}\,\frac{n^2}{\sin^2\frac{\theta}{2}}$.

(A.7)

$$\frac{\sigma(\theta)}{\sigma_c(\theta)} = \left|\, ie^{-in\ln\,\sin^2\frac{\theta}{2}} + \frac{\sin^2\frac{\theta}{2}}{n}\sum_{\ell=0}^{\infty}(2\ell+1)\, e^{2i(\sigma_\ell-\sigma_0)}\left(1-A_\ell e^{2i\delta_\ell}\right)P_\ell(\cos\theta)\right|^2$$

$$= \Big| \, i \cos(n \ln \, \sin^2 \frac{\theta}{2}) + \sin (n \ln \sin^2 \frac{\theta}{2})$$

$$+ \frac{\sin^2 \frac{\theta}{2}}{n} \sum_{\ell=0}^{\infty} (2\ell+1) \cos 2 (\sigma_\ell - \sigma_0) \, P_\ell \, (\cos \theta)$$

$$+ \frac{\sin^2 \frac{\theta}{2}}{n} \sum_{\ell=0}^{\infty} (2\ell+1) \, A_\ell \, \cos 2(\sigma_\ell - \sigma_0 + \delta_\ell) \, P_\ell \cos \theta)$$

$$+ \frac{i \sin^2 \frac{\theta}{2}}{n} \sum_{\ell=0}^{\infty} (2\ell+1) \, \sin 2 \, (\sigma_\ell - \sigma_0) \, P_\ell$$

$$+ \frac{- i \sin^2 \frac{\theta}{2}}{n} \sum_{\ell=0}^{\infty} (2\ell+1) \, A_\ell \, \sin 2(\sigma_\ell - \sigma_0 + \delta_\ell) \, P_\ell \, (\cos \theta) \Big|^2 .$$

$$\frac{\sigma(\theta)}{\sigma_c(\theta)} = \left\{ \cos (n \ln \sin^2 \frac{\theta}{2}) + \frac{\sin^2 \frac{\theta}{2}}{n} \right. \times$$

$$\left. \sum_{\ell=0}^{\infty} (2\ell+1) \left[\sin 2(\sigma_\ell - \sigma_0) - A_\ell \, \sin 2 (\sigma_\ell - \sigma_0 + \delta_\ell) \right] P_\ell(\cos \theta) \right\}^2 +$$

$$+ \left\{ \sin(n \ln \sin^2 \frac{\theta}{2}) + \frac{\sin^2 \frac{\theta}{2}}{n} \right. \times$$

$$\left. \sum_{\ell=0}^{\infty} (2\ell+1) \left[\cos 2(\sigma_\ell - \sigma_0) - A_\ell \cos 2 (\sigma_\ell - \sigma_0 + \delta_\ell) \right] P_\ell(\cos \theta) \right\}^2 .$$

(A.8)

In the Blair sharp-cutoff model,

$$\eta_\ell = A_\ell \, e^{2i(\sigma_\ell + \delta_\ell)}$$

where

$$\begin{aligned} A_\ell &= 0, && \text{for} \quad \ell \leq \ell' ; \\ A_\ell &= 0, && \text{for} \quad \ell > \ell' ; \\ \delta_\ell &= 0, && \text{for all} \quad \ell ; \end{aligned} \qquad \text{(A.9)}$$

Substituting (A.9) in (A.8) gives formula (1.9) of the text.

For the Coulomb phase shifts the following relation was used:

$$\sigma_\ell = \sigma_0 + \sum_{k=1}^{\ell} \text{arc tan} \frac{n}{k} = \arg \Gamma(1 + \ell + in).$$

```
      PROGRAM FUZZED - BY J.ALSTER (4601-50)
      ZT= CHARGE OF TARGET
      ZP= CHARGE OF PROJECTILE
       T= C.O.M. ENERGY
      TARGET= MASS OF TARGET
      PROJEC= MASS OF PROJECTILE
      TETAIN= FIRST ANGLE TO BE CALCULATED
      NFIN= NUMBER OF ANGLES
      NFIN= NUMBER OF ANGLES
      DTETA=  ANGLE INCREMENT
      EXPER(N)= EXPERIMENTAL CROSS SECTION
      CRIT= MAXIMUM OF SUM OF DEVIATIONS
      ELLAI  = FIRST L-SUB-A VALUE
      DELLA  = INCREMENT IN L-SUB-A
      KFIN   = NUMBER OF L-SUB-A VALUES
      DLTLAI= FIRST DELTA-L-SUB-A VALUE
      DDLTLA= ANALOGOUS TO DELLA
      IFIN  = ANALOGOUS TO KFIN
      DELTA+= FIRST DELTA VALUE
      DDELTA= ANALOGOUS TO DELLA
      JFIN  = ANALOGOUS TO KFIN
      ELDLTI= FIRST L-SUB-DELTA VALUE
      DLDELT= ANALOGOUS TO DELLA
      MAFIN = ANALOGOUS TO KFIN
      DLTDLI= FIRST DELTA-L-SUB-DELTA VALUE
      DDLTDL= ANALOGOUS TO DELLA
      MBFIN = ANALOGOUS TO KFIN
      DIMENSION A(250),TERM(250),SIGMA(250),DSUB(250),SINTER(250),COSTER
     X(250),POL(250),T1T(250),T2T(250),ELLA(10),DELTLA(10),DELTA(10),ELD
     XELT(10),DELTDL(10),TETAR(180),RUTHER(180),CROSEC(180),DIFSQ(180),
     XEXPER(180),ABSCRS(180),NTETA(180),MROS(180),MEXP(180) ,AAA(250)
   10 READ 300,ZT,ZP,T,TARGET,PROJEC,TETAIN,NFIN,DTETA
 1020 DO 1025 N=1,NFIN
 1025 READ 306,EXPER(N)
 1016 READ 302,CRIT,MODE
   11 READ301,ELLAI,DELLA,KFIN
   12 READ301,DLTLAI,DDLTLA,IFIN
   13  READ301,DELTAI,DDELTA,JFIN
 1013 IF(SENSE SWITCH2)14,30
   14 READ301,ELDLTI,DLDELT,MAFIN
   15 READ301,DLTDLI,DDLTDL,MBFIN
   30 TARMAS=0.16598E-23*TARGET
   31 PROMAS=0.16598E-23*PROJEC
   32 E=0.1602E-05*T
   33 ZZOE=(ZT*ZP/T)**2*0.001298
   34 REDMAS=(TARMAS*PROMAS)/(TARMAS+PROMAS)
   35 VELOC=SQRTF(2.*E/REDMAS)
   36 CLASSP=(ZT*ZP*0.21877E+09)/VELOC
 1036 BROG=0.105443E-26/(REDMAS*VELOC)
   37 WRITE OUTPUT TAPE 5,310,ZT,ZP,T,TARGET,PROJEC,BROG,CLASSP
   40 TERM(1)=0.
   41 DO 43 L=2,200
   42 ELL=L-1
   43 TERM(L)=ATANF(CLASSP/ELL)
   50 SIGMA(1)=TERM(1)
   51 DO 52 L=1,199
   52 SIGMA(L+1)=SIGMA(L)+TERM(L+1)
   60 ELLA(1)=ELLAI
   61 DELTLA(1)=DLTLAI
   62 DELTA(1)=DELTAI
 1062 IF(SENSE SWITCH2)63,70
   63 ELDELT(1)=ELDLTI
   64 DELTDL(1)=DLTDLI
```

```
  70 DO260 K=1,KFIN
  75 ELLA(K+1)=ELLA(K)+DELLA
  80 DO260 I=1,IFIN
  84 AB=0.
  85 DELTLA(I+1)=DELTLA(I)+DDLTLA
  86 DO 90 L=1,250
  87 ELL=L-1
  88 A(L)=1./(1.+EXPF((ELLA(K)-ELL)/DELTLA(I)))
1088 AAA(L)=(2.*ELL+1.)*(1.-A(L)**2)
1089 AB=AB+AAA(L)
  89 IF(A(L)-.9999)90,90,91
  90 CONTINUE
  91 LFIN=ELL+1.00001
  92 DAB=3.14159*BROG**2*AB
  94 DO260 J=1,JFIN
  95 DELTA(J+1)=DELTA(J)+DDELTA
1096 IF(SENSE SWITCH2)100,1097
1097 MAFIN=1
1098  ELD ELT(1)=0.
1099 DLDELT=0.
1100 MBFIN=1
1101 DELTDL(1)=0.
1102 DDLTDL=0.
 100 DO260 MA=1,MAFIN
 105 ELDELT(MA+1)=ELDELT(MA)+DLDELT
 110 DO260 MB=1,MBFIN
 115 DELTDL(MB+1)=DELTDL(MB)+DDLTDL
 140 DO 1149 L=1,LFIN
 142 ELL=L-1
1143 IF(SENSE SWITCH2)144,1145
 144 DSUB(L)=DELTA(J)/(1.+EXPF((ELL-ELDELT(MA))/DELWDL(MB)))
 145 GO TO 1149
1145 DSUB(L)=DELTA(J)/(1.+EXPF((ELL-ELLA(K))/DELTLA(I)))
1149 CONTINUE
 150 DO156 L=1,LFIN
 152 AA=2*L-1
 154 SINTER(L)=AA*(SINF(2.*SIGMA(L))-A(L)*SINF(2.*SIGMA(L)+2.*DSUB(L)))
 156 COSTER(L)=AA*(COSF(2.*SIGMA(L))-A(L)*COSF(2.*SIGMA(L)+2.*DSUB(L)))
 157 IF(SENSE SWITCH 3)1157,160
1157 WRITE OUTPUT TAPE 4,310,ZT,ZP,T,TARGET,PROJEC,BROG,CLASSP
 158 IF(SENSE SWITCH 2)1159,1160
1159 WRITE OUTPUT TAPE 4,315,ELLA(K),DELTLA(I),DELTA(J),ELDELT(MA),
    XDELTDL(MB),LFIN
     GO TO 1161
1160 WRITE OUTPUT TAPE 4,315,ELLA(K),DELTLA(I),DELTA(J),ELLA(K),
    XDELTLA(I),LFIN
1161 WRITE OUTPUT TAPE 4,328
     DO 159 L=1,LFIN
     ELL=L-1
 159 WRITE OUTPUT TAPE 4,329,ELL,A(L),AAA(L),SIGMA(L),DSUB(L)
 160 TETAR(1)=0.01745*TETAIN
 164 DEVSQ=0.
 165 DO230 N=1,NFIN
 168 TETAR(N+1)=TETAR(N)+0.01745 *DTETA
 170 NTETA(N)=57.31*TETAR(N)
 172 X=COSF(TETAR(N))
 174 POL(1)=PLGNF(X)
 176 DO 178 L=2,LFIN
 178 POL(L)=PLGMF(X)
```

```
 182 C=(SINF(TETAR(N)/2.))**2
 184 CC=CLASSP*LOGF(C)
 186 COSCC=COSF(CC)
 188 SINCC=SINF(CC)
 190 CSQ=C**2
 192 RUTHER(N)=ZZOE/CSQ
 196 SINSUM=0.
 197 COSSUM=0.
 200 DO205 L=1,LFIN
 202 T1T(L)=SINTER(L)*POL(L)
 203 T2T(L)=COSTER(L)*POL(L)
 204 SINSUM=SINSUM+T1T(L)
 205 COSSUM=COSSUM+T2T(L)
 210 CROSS1=COSCC+C*SINSUM/CLASSP
 212 CROSS2=SINCC+C*COSSUM/CLASSP
 214 CROSEC(N)=CROSS1**2+CROSS2**2
 216 ABSCRS(N)=RUTHER(N)*CROSEC(N)
 218 DIFSQ(N)=SQRTF(((CROSEC(N)-EXPER(N))/EXPER(N))**2)*100.
 230 DEVSQ=DEVSQ+DIFSQ(N)
 243 IF(DEVSQ-CRIT)244,244,1231
1231 IF(SENSE SWITCH2)240,1241
 240 WRITE OUTPUT TAPE 5,315,ELLA(K),DELTLA(I),DELTA(J),ELDELT(MA),
    XDELTDL(MB),LFIN
      GO TO 242
1241 WRITE OUTPUT TAPE 5,315,ELLA(K),DELTLA(I),DELTA(J),ELLA(K),
    XDELTLA(I),LFIN
 242 WRITE OUTPUT TAPE 5,316,DEVSQ,CRIT,DAB
     GO TO 260
 244 IF(SENSE SWITCH1)245,6000
 245 WRITE OUTPUT TAPE 5,310,ZT,ZP,T,TARGET,PROJEC, BROG,CLASSP
1245 IF(SENSE SWITCH2)1246,1247
1246 WRITE OUTPUT TAPE 5,315,ELLA(K),DELTLA(I),DELTA(J),ELDELT(MA),
    XDELTDL(MB),LFIN
      GO TO 3246
1247 WRITE OUTPUT TAPE 5,315,ELLA(K),DELTLA(I),DELTA(J),ELLA(K),
    XDELTLA(I),LFIN
3246 WRITE OUTPUT TAPE 5,316,DEVSQ,CRIT,DAB
 246 WRITE OUTPUT TAPE 5,319
 247 DO250 N=1,NFIN
 250 WRITE OUTPUT TAPE 5,320,NTETA(N),CROSEC(N),RUTHER(N),ABSCRS(N)
 251 WRITE OUTPUT TAPE 5,321
6000 IF(SENSE SWITCH 6)5000,260
5000 WRITE OUTPUT TAPE 3,310,ZT,ZP,T,TARGET,PROJEC,BROG,CLASSP
     IF(SENSE SWITCH 2)5001,5002
5001 WRITE OUTPUT TAPE 3,315,ELLA(K),DELTLA(I),DELTA(J),ELDELT(MA),
    XDELTDL(MB),LFIN
     WRITE OUTPUT TAPE 3,316,DEVSQ,CRIT,DAB
     GO TO 5004
5002 WRITE OUTPUT TAPE 3,315,ELLA(K),DELTLA(I),DELTA(J),ELLA(K),
    XDELTLA(I),LFIN
     WRITE OUTPUT TAPE 3,316,DEVSQ,CRIT,DAB
5004 WRITE OUTPUT TAPE 3,5025
5005 DO 5010 N=1,NFIN
5006 MROS(N)=28.9504*LOGF(100.*  CROSEC(N))      +30.
5007 MEXP(N)=28.9504*LOGF(100.*  EXPER(N))    +30.
5008 WRITE OUTPUT TAPE 3,5030,CROSEC(N),NTETA(N)
5009 CALLGRAPH(MROS(N),3,1H*)
5010 CALLGRAPH(MEXP(N),3,1H+)
     WRITE OUTPUT TAPE 3,5025
```

```
5020 FORMAT(17X,2H I,18X,2H I,18X,2H I,18X,2H I,18X,2H I,18X,2H I   )
5025 FORMAT(120H CROSEC     ANGLE ......................................
    X................................................................)
5030 FORMAT(F11.7,I5,3H  .,99X,2H .  )
 260 CONTINUE
 270 IF(MODE-1)275,1016,10
 275 ENDFILE5
 276 REWIND 5
     IF(SENSE SWITCH 6)277,278
 277 END FILE 3
     REWIND 3
 278 IF(SENSE SWITCH 3)279,350
 279 END FILE 4
     REWIND 4
 300 FORMAT(2F5.1,3F9.4,F6.1,I4,F5.1)
 301 FORMAT(F7.2,F6.2,I3)
 302 FORMAT(F9.0,I2)
 306 FORMAT(F10.7)
 310 FORMAT(6H1  ZT=F6.1,7H    ZP=F6.1,5H   E=F13.5,11H    TARMAS=F13.5
    X,10H   PROMAS=F13.5/17H   DEBROGLIE/2PI=E13.5,4H CM.,5X,9H  CLASSP
    X=F11.4          //)
 315 FORMAT( 8H   ELLA=F6.1,10H   DELTLA=F7.3, 9H   DELTA=F7.3,
    X10H   ELDELT=F6.1,10H   DELTDL=F7.3, 9H    LFIN=I4)
 316 FORMAT(28H SUM SQUARE OF CROSEC-EXPER=F10.0,7H  CRIT=F10.0,32H
    XTOTAL REACTION CROSSSECTION=E12.5,6H CM**2        //)
 319 FORMAT(118H THETA IN DEGREES                    CROSS-SECTION
    X    RUTHERFORD IN BARNS    ABSOLUTE CROSS-SECTION IN BARNS
 320 FORMAT(I10,3E35.7)
 321 FORMAT(1H1)
 325 FORMAT(I4)
 328 FORMAT(7X,3H L ,11X,9H A(L)     ,18H (2L+1)(1-A(L)**2),11X,9H SIGMA
    X(L),11X,8H DSUB(L)       //)
 329 FORMAT(F10.0,4E20.6)
 350 STOP
 400 END(0,1,0,0,1)
```

ACKNOWLEDGMENTS

I take particular pleasure in thanking:

Dr. Homer E. Conzett for suggesting the experiment and for his guiding cooperation;

Dr. Bernard G. Harvey for his support and encouragement;

Professor I. Perlman and Professor John O. Rasmussen for their hospitality during my stay at the Lawrence Radiation Laboratory;

Professor A. H. Wapstra for his encouragement and valuable criticism during the preparation of this manuscript;

Dr. Jose Gonzales-Vidal, Dr. George Igo, Dr. Alfred E. Glassgold, Dr. John R. Morton III, James F. Mollenauer, and Joseph Cerny III for valuable discussions;

Dr. George Igo for making available his detailed optical-model computations;

Jack H. Elliott for the preparation of the solid-state radiation detector;

Dan O'Connell for the preparations of thin films.

The personnel of the heavy-ion linear accelerator for their cooperation.

Above all, a special acknowledgment of gratitude is owing to my wife for her patience and understanding during the course of this work.

This work was done under the auspices of the U. S. Atomic Energy Commission.

REFERENCES

1. E. J. Williams, Rev. Modern Phys. 17, 217 (1945).
2. J. S. Blair, Phys, Rev. 95, 1218 (1954).
3. D. D. Kerlee, J. S. Blair, and G. W. Farwell, Phys. Rev. 107, 1343 (1957).
4. J. S. Blair, Phys. Rev. 108, 827 (1957).
5. J. S. Blair, open letter to J. McIntyre, 1957.
6. G. Breit, M. H. Hull, and R. L. Gluckstern, Phys. Rev. 87, 74 (1952).
7. J. H. Fremlin, Nuclear Reactions, ed. by P. M. Endt and M. Demeur, Vol. 1 (North-Holland Publishing Co., Amsterdam, 1959), Chap. 3.
8. Proceedings of the Conference on Reactions between Complex Nuclei, Gatlinburg, Tennessee, Oak Ridge National Laboratory Report ORNL-2606 (unpublished).
9. Proceedings of the Second Conference on Reactions between Complex Nuclei, Gatlinburg, Tennessee (John Wiley & Sons, Inc., New York, 1960).
10. A. Zucker, Nuclear Interactions of Heavy Ions, Annual Review of Nuclear Science, 1960.
11. R. Evans, The Atomic Nucleus (McGraw-Hill Book Co., New York, 1955), Appendix B.
12. L. I. Schiff, Quantum Mechanics (McGraw-Hill Book Co., New York, 1955.
13. N. S. Wall, J. R. Rees, and K. W. Ford, Phys, Rev. 97, 726 (1955).
14. R. E. Ellis and L. Schecter, Phys. Rev. 101, 636 (1956).
15. J. A. McIntyre, K. H. Wang, and L. C. Becker, Phys. Rev. 117, 1337 (1960).
16. J. A. McIntyre, S. D. Baker, and K. H. Wang, Ref. 9, p. 180.
17. J. M. Blatt and V. F. Weisskopf, Theoretical Nuclear Physics (John Wiley & Sons, Inc., New York, 1952).
18. J. Alster and H. E. Conzett, Ref. 9, p. 175.
19. J. A. McIntyre, Proceedings of the International Conference on Nuclear Structure, Kingston, Canada, ed. by Bromley and Vogt (University of Toronto Press, 1960).
20. E. Hubbard et al., to be published in Rev. Sci. Instr.
21. A. R. Quinton, C. E. Anderson, and W. J. Knox, Phys. Rev. 115, 886, (1959).

22. A. E. Larsh, G. E. Gordon, and T. Sikkeland, Rev. Sci. Instr. 31, 1114 (1960).
23. H. W. Schmitt, J. H. Weiler, F. J. Walter, and R. J. Silva, Bull. Am. Phys. Soc., Ser. II, 6 (April 24, 1961).
24. The detector was made by Jack H. Elliott, Lawrence Radiation Laboratory, Berkeley.
25. F. S. Goulding and W. L. Hansen, to be published in Nuclear Instr.
26. E. Fairstein, Rev. Sci. Instr. 27, 475 (1956).
27. The In and Ag targets were prepared by Daniel O'Connell, Lawrence Radiation Laboratory, Berkeley.
28. The nickel foils were obtained from McKay Company, New York.
29. K. B. Mather and P. Swan, Nuclear Scattering (Cambridge University Press, 1955), p. 28.
30. C. L. Critchfield and D. C. Dodder, Phys, Rev. 75, 419 (1949).
31. G. Breit, H. M. Thaxton, and L. Eisenbud, Phys. Rev. 55, 1018 (1939).
32. E. Fermi, Nuclear Physics, ed. by J. Orear et al. (University of Chicago Press, 1959).
33. E. Williams, Proc. Roy Soc. (London) A169, 531 (1939).
34. H. L. Reynolds and A. Zucker, Phys. Rev. 102, 1378 (1956).
35. M. L. Halbert and A. Zucker, Phys. Rev. 115, 1635 (1959).
36. M. L. Halbert, C. E. Hunting, and A. Zucker, Phys. Rev. 117, 1545 (1960).
37. M. L. Halbert and A. Zucker, Nuclear Phys. 16, 158 (1960).
38. E. Goldberg and H. L. Reynolds, Phys. Rev. 112, 1981 (1958).
39. D. D. Kerlee, H. L. Reynolds, and E. Goldberg, Phys. Rev. 119, 2009 (1960).
40. J. A. McIntyre, S. D. Baker, and T. L. Watt, Phys. Rev. 116, 1212 (1959).
41. Ref. 17, p. 345-350.
42. K. W. Ford and J. A. Wheeler, Ann. Phys. 7, 259 (1959).
43. M. V. Goldman, Oak Ridge National Laboratory Report ORNL-3025, 1961 (unpublished).
44. R. M. Eisberg and C. E. Porter, to be published in Rev. Mod. Phys.
45. K. C. van der Hulst, Scattering of Light by Small Particles (John Wiley & Sons, New York, 1957).
46. A. E. Glassgold, W. B. Cheston, M. L. Stein, S. B. Schuldt, and J. W. Ericson, Phys. Rev. 106, 1207 (1957).
47. A. E. Glassgold and P. J. Kellogg, Phys. Rev. 107, 1372 (1957).

48. M. A. Melkanoff, J. S. Nodvik, P. S. Saxon, and R. W. Woods, Phys. Rev. 106, 793 (1957).
49. W. B. Cheston and A. E. Glassgold, Phys. Rev. 106, 1215 (1957).
50. G. Igo and R. M. Thaler, Phys. Rev. 106, 126 (1957).
51. C. E. Porter, Phys. Rev. 112, 1722 (1958).
52. R. H. Bassel and R. M. Drisko, Ref. 19, p. 212.
53. L. Seidlitz, E. Bleuler, and D. J. Tendam, Phys. Rev. 110, 682 (1958).
54. G. Igo, H. E. Wegner, and R. M. Eisberg, Phys. Rev. 101, 1508 (1956).
55. G. Igo, Phys. Rev. 115, 1665 (1959).
56. This factor is often called "transmission factor."
57. A similar plot for T_ℓ has been given by Cheston and Glassgold as a justification for the Blair model.